Low-Reynolds-number wake of three tandem elliptic cylinders

Viet Dung Duong (Dương Việt Dũng)[1*], Van Duc Nguyen (Nguyễn Văn Đức)[1],
Van Tien Nguyen (Nguyễn Văn Tiến)[2], Ich Long Ngo (Ngô Ích Long)[3]
[1]School of Aerospace Engineering, University of Engineering and Technology,
Vietnam National University, Ha Noi City, Vietnam
[2]Department of Aerospace Engineering, Pusan National University, Busan, Republic of Korea
[3]School of Mechanical Engineering, Hanoi University of Science and Technology,
No. 01, Dai Co Viet, Hai Ba Trung, Hanoi, Vietnam

Abstract

The flow around three elliptic cylinders with equal spacing and aspect ratio in tandem arrangements was numerically investigated through direct numerical simulation. The spacing ratio (L/D, where D and L are the major axis and the center-to-center distance of two adjacent elliptic cylinders, respectively) ranging from 1.5 to 10 and the Reynolds numbers of $Re = 65 - 160$ (based on D) are examined. The analysis aims at the effects of L/D and Re on wake structures, hydrodynamic forces, and Strouhal numbers and correlates them with the underlying flow physics. The flow is highly changeable to Re and L/D, classifying into five distinct regimes, namely meandering, overshoot, reattachment, quasi-coshedding, and coshedding. Two vortex shedding frequencies for middle and downstream cylinders are observed in the latter two regimes, indicating the significant wake interference, where three vortex shedding modes are spatially observed including primary, two-layered, and secondary. The transition between two adjacent modes forms two boundaries. At the first boundary, vortices divert from the cylinder centerline and follow two layers; while the vortices converge the cylinder centerline at the second boundary. The first boundary location is not stationary at $Re = 65 - 100$; while it is stationary at $Re = 160$. Otherwise, the second boundary location moves upstream with an increase in L/D; while the range of movement decreases with an increase in Re. The increase in Re advances the disturbance level and urges the transition between vortex shedding modes. The time-mean lift and drag coefficients for three cylinders are highly sensitive with an increase in L/D.

Keywords: wakes, vortex streets, laminar flow, vortex instability, direct numerical simulation

1 Introduction

Cluster of cylindrical structures (more than two objects e.g. tube bundles of heat exchanger, offshore risers, and pipe-rack) are more regularly encountered in engineering applications than isolated structure, although hydrodynamics research of these cluster systems has rarely been conducted.[1–8] For simplicity, flow past two cylinders in tandem arrangement has been considered as the archetypal idealization of the multiple structures because this flow includes most well-known flow features, such as separation, reattachment, recirculation, quasi-periodic vortex shedding.[9–11] Therefore, more attention

*Corresponding author: duongdv@vnu.edu.vn

has been paid to this flow for decades while the flow past three tandem cylinders has seldom been elucidated. Otherwise, flow direction to a tube is not always perpendicular to the tube axis, thus forming an ellipse cross-section of a tube in such an orientation. The elliptic cylinders (intermediate geometries between flat plates and circular cylinders) are broadly utilized in the industries due to the considerable importance of heat loads and limited space; and in comparison with a circular cylinder, an elliptic cylinder provides lower drag force and higher heat transfer.[12] In this paper, characteristics of flow past three elliptic cylinders in tandem arrangements, including hydrodynamic coefficients, spectral analysis, and wake structures, are carried out in a wide parametric space for a comprehensive understanding of the underlying fluid dynamics.

Due to complex interactions among separated shear layers, vortices, and bluff bodies, the flow around two tandem circular cylinders is firstly discussed. The flow is categorized into three distinct regimes, such as single bluff-body, reattachement, and co-shedding.[13–18] These regimes intermittently occur in the gap between two cylinders and in the wake of the downstream cylinder. The variation of spacing ratio L/D, where L is the center-to-center spacing of cylinders and D is the cylinder diameter, significantly influences the transformation of these regimes.[19,20] At the range of $L/D < 1.3 - 1.7$, the single bluff-body regime appears; two cylinders are closely arranged as a single body that the stagnant flow in the gap appears; and the separated shear layer of the upstream cylinder overshoots the downstream one. The reattachment regime occurs at $1.3 - 1.7 < L/D < 3.5 - 3.9$, where the separated shear layers reattach continuously/alternately to the frontal surface of the downstream cylinder; and quasi-steady flow appears in the gap. In the co-shedding regime ($L/D > 3.5 - 3.9$), the unsteady flow appears in the gap that the separated shear layer alternately rolls up the downstream cylinder; and vortices are generated simultaneously from two cylinders. Furthermore, the critical spacing $(L/D)_c$ is the key quantity to determine the location of transformation between reattachment and co-shedding regimes.[21–25] Several factors, such as Reynolds number ($Re = U_\infty D/\nu$, where U_∞ is the freestream velocity and ν is the kinematic viscosity of the fluid), L/D, inflow turbulence intensity, and three-dimensionality of flow, affect the quantity, thus inducing the hysteresis transformation of the two regimes.[26–30] As the reattachment transforms into the co-shedding, the time-averaged drag force of the downstream cylinder jumps from negative to positive value, termed as the drag inversion. The occurrence of the drag inversion is because of the shadowing effect even at large L/D that the downstream cylinder interferes with the vortices shed from the upstream cylinder.[31–34] However, the other effect, at which downstream cylinder modifies the wake topology of the upstream one causing the drag reduction of the upstream cylinder, is perceivable at sufficiently small L/D, for example $L/D < 5$ for two tandem circular cylinders[10,20] and $L/D < 8$ for three tandem circular cylinders.[35]

In engineering devices and systems, the diameters of tandem cylindrical structures are not necessarily identical depending on the enhancements of flow control.[36,37] Accordingly, the upstream cylinder with a smaller diameter is used to control the vortices shed from the downstream cylinder. Hence, the physics of flow past two tandem circular cylinders with unequal diameters are significantly affected by the diameter ratio of cylinder d/D (where d and D are diameters of the upstream and downstream cylinder, respectively), spacing ratio, and Reynolds number.[38,39] Wang et al.[40] and Alam et al.[41] experimentally investigated the turbulence effect on the wake structures of upstream and downstream cylinders at $Re = (0.8 - 4.27) \times 10^4$, $d/D = 0.25 - 1.0$, and $L/D = 5.5 - 20$. The hydrodynamic coefficients of the downstream cylinder are more significantly influenced by L/D than by d/D. Shan[42] numerically scrutinized the wake structures of upstream and downstream cylinders at $Re = 100 - 150$,

$d/D = 0.4 - 1.0$ and $L/D = 1.0 - 8.0$. He reported that the co-shedding regime is subdivided into three vortex shedding modes, such as primary, two-layered, and secondary. In the secondary vortex shedding mode, the fundamental vortex and subharmonic frequencies are identified.

Furthermore, the flow physics of single or two tandem elliptic cylinders deviate significantly from those of single or two tandem circular cylinders due to the geometric difference and orientation of the elliptic cylinder with inflow direction. With the variation of elliptic cylinder's aspect ratio (AR) and angle of attack (γ), Shi et al.[43] observed three distinct structures of wake behind a single elliptic cylinder at $Re = 150$, including steady wake ($AR < 0.37$, $\gamma < 2.5^0$), Karman wake followed by steady wake ($AR \geq 0.37 - 0.67$, depending on γ), and Karman wake followed by secondary wake ($AR \leq 0.67$, $\gamma > 52^0$). Pulletikurthi et al.[44] conducted the simulation of the flow past a single elliptic cylinder at $Re = 130$, $AR = 0.4$ and $\gamma = 90^0$ to investigate the wake transition between primary and secondary vortex shedding modes. They pointed out the irregularity of the transition process, which supports the transmutation of the wavelength of the vortex structures. Zhu et al.[45] investigated the effect of near and moving flat wall on the transition between vortex shedding modes behind the single elliptic cylinder at $Re = 40 - 200$. They found that the transition increases with a decrease in gap ratio (G/D, where G is the distance between the cylinder and the wall). Zhu et al.[46] further scrutinized the moving wall effect on the separation and stagnation points of a single elliptic cylinder at $Re = 5 - 150$; while Zhu et al[47] examined the three-dimensionality effect on the wake transition at $Re = 100 - 200$, classifying into three distinct flow patterns: Karman, two-layered, and three-dimensional vortex pairs. Wu et al.[48] numerically scrutinized the wake transition of flow past two tandem elliptic cylinders with an aspect ratio ($AR = 0.7 - 1.5$) to characterize the structural response of upstream and downstream cylinders at a small spacing ratio ($L/D = 2 - 11$). The flow regimes are observed and classified into steady, reattachment and two-layered, and two-layered and co-shedding.

To the best of the authors' knowledge, the aforementioned studies have been mainly conducted for wake interference of two tandem elliptic cylinders, while that of three tandem elliptic cylinders has not been clarified. Particularly, in two tandem elliptic cylinders,[49] the secondary vortex structures fully developed in the far wake show the small effect on the hydrodynamic performance of the downstream cylinder. However, these structures might occur in the near wake of three tandem elliptic cylinders, thus influencing significantly the hydrodynamics of the downstream cylinder. In addition, the previous investigations were performed under either subcritical Re or narrow range of L/D, such examinations are relatively insufficient. At low Re, the features of underlying physical mechanism of the wake are revealed more quantitatively by disregarding the turbulence distortion. Naturally, the unknown flow features of three tandem elliptic cylinders must be raised by some questions: (1) How do the wake structures and characteristics of the flow change with the simultaneous variations of L/D and Re? (2) What are the significant effects on the hydrodynamics of the downstream cylinder between low Re and subcritical Re? (3) How are the boundaries separating three vortex shedding structures (primary, two-layered, secondary) determined in the wake? And (4) what physical mechanisms affect the formation of these boundaries? Therefore, the originality of this paper is to answer these questions. The comprehensive numerical analysis of flow past three tandem elliptic cylinders is qualitatively and quantitatively conducted in a space of $Re = 65 - 160$ and $L/D = 1.5 - 10$ with an interval of 0.5. This range of low Reynolds numbers eliminates the turbulence caused by flow distortion, thus ensuring physically two-dimensional vortex dynamics.[50] The interval of 0.5 is sufficiently small to capture the sensitivity of flow structures and hydrodynamic forces.[35]

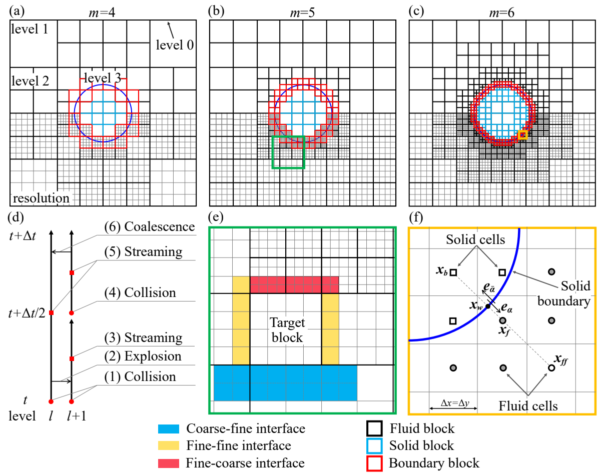

Figure 1: Block-structured topology-confined mesh refinement with four levels (a), five levels (b), and six levels (c); upper and lower half-domains present for block and cell structures, respectively. (d) The computation steps for two refinement levels. (e) Exchange of information between neighbouring blocks. (f) Interpolated bounce-back boundary condition.

The rest of this paper is organized as follows. Section 2 expresses the governing equations and numerical method based on the lattice Boltzmann method combined with block-structured topology-confined mesh refinement. The flow configurations and computational setup are discussed in section 3. Section 4 inspects the effect of L/D on the wake structures and hydrodynamics; while section 5 presents the effect of Reynolds number on the characteristics of near and intermediate wake structures. Flow dependence on Re and L/D is discussed in section 6 before the major conclusions summarized in section 7.

2 Governing equations and numerical methods

The macroscopic variables of the incompressible flow are solved by employing the lattice Boltzmann method (LBM) for fluid domain, while the interpolated bounce-back enforcement is used for interaction between fluid and solid boundary with the second-order accuracy. To improve the stability of the numerical scheme, the multiple-relaxation-time scheme is used. In order to accelerate the computation, the block-structured topology-confined mesh refinement is employed to distribute the fine mesh on the high-velocity-gradient region around the solid boundary and the coarse mesh on the low-velocity-gradient region. The details of these numerical methods are expressed by the following subsections.

2.1 Lattice Boltzman method for incompressible flows

In LBM, the particles, regularly located in a lattice, experience collision followed by streaming. In the present study, the LBM approach proposed by Chen and Doole[51] is employed and expressed as

$$f_\alpha\left(\boldsymbol{x}+\boldsymbol{e}_\alpha \Delta t, t+\Delta t\right)=f_\alpha(\boldsymbol{x}, t)+\Omega_\alpha(\boldsymbol{x}, t) \tag{1}$$

where $f_\alpha(\boldsymbol{x},t)$ is the distribution function of particle velocity along the αth direction, $\Omega_\alpha(\boldsymbol{x},t)$ is an operator representing the change rate of f_α resulting from collision. In this study, the D2Q9 lattice, which has 9 particles arranged regularly in a square configuration, is utilized. The time step Δt and lattice size Δx represent a temporal and spatial resolution, respectively. This interprets that at the time $(t+\Delta t)$, particles $f_\alpha(\boldsymbol{x},t)$ convect with their velocities $\boldsymbol{e}_\alpha$ to neighbouring points $(\boldsymbol{x}+\boldsymbol{e}_\alpha\Delta t)$. In the velocity sets of D2Q9, the velocities of particles are formulated as:

$$\boldsymbol{e}_\alpha = \begin{cases} (0,0), & \alpha = 0 \\ \left(\cos\left(\frac{(\alpha-1)\pi}{4}\right), \sin\left(\frac{(\alpha-1)\pi}{4}\right)\right), & \alpha = 1,2,3,4, \\ \sqrt{2}\left(\cos\left(\frac{(\alpha-1)\pi}{4}\right), \sin\left(\frac{(\alpha-1)\pi}{4}\right)\right), & \alpha = 5,6,7,8. \end{cases} \tag{2}$$

In the right-hand side of equation (1), the particles residing in the lattice are relaxed towards the equilibrium with the same relaxation time. The equation (1) is decomposed into two separated parts, including collision and streaming. The collision part is written as:

$$f_\alpha^+(\boldsymbol{x},t) = f_\alpha(\boldsymbol{x},t) + \Omega_\alpha(\boldsymbol{x},t) \tag{3}$$

where $f_\alpha^+(\boldsymbol{x},t)$ are the distribution functions of post collision. The common collision operator of Bhatnagar-Gross-Krook, reported substantially by Chen and Doolen,[51] implements the dynamics of relaxation towards a local equilibrium with a relaxation parameter $\omega = \Delta t/\tau$. Inserting Bhatnagar-Gross-Krook collision operator $\Omega_\alpha^{BGK}(\boldsymbol{x},t) = -\omega\left(f_\alpha(\boldsymbol{x},t) - f_\alpha^{eq}(\boldsymbol{x},t)\right)$ into equation (3) it can be rewritten as

$$f_\alpha^+(\boldsymbol{x},t) = f_\alpha(\boldsymbol{x},t) - \frac{\Delta t}{\tau}\left(f_\alpha(\boldsymbol{x},t) - f_\alpha^{eq}(\boldsymbol{x},t)\right) \tag{4}$$

where τ is the single relaxation time. It is well understood that the only condition one must satisfy in numerical simulations of incompressible flow is $M << 1$, where M is the Mach number. As a result, the density is approximately a constant, and the density fluctuation is neglected. Hence, f_α^{eq} is the distribution of equilibrium and defined as

$$f_\alpha^{eq} = \rho w_\alpha\left(1 + \frac{\boldsymbol{e}_\alpha \boldsymbol{u}}{c_s^2} + \frac{\boldsymbol{Q}_\alpha : \boldsymbol{u}\boldsymbol{u}}{2c_s^4}\right) \tag{5}$$

where the tensor $\boldsymbol{Q}_\alpha = \boldsymbol{e}_\alpha\boldsymbol{e}_\alpha - c_s^2\boldsymbol{I}$, here $c_s = 1/\sqrt{3}$ is the sound speed of lattice, and w_α are the lattice weights related to discrete analogs of the absolute Maxwell distribution. The above distribution function is the equilibrium distribution function of the incompressible lattice Boltzmann model, which is fully consistent with the second order small velocity expansion in the Chapman-Enskog analysis of LBE models. Through the Chapman-Enskog procedure, the condition for incompressible flow, $\nabla\cdot\boldsymbol{u} = 0$, is exactly satisfied in the case of steady flow. In the D2Q9 model, the lattice weights are given as $w_0 = 4/9$, $w_\alpha = 1/9$ for $\alpha = 1-4$, and $w_\alpha = 1/36$ for $\alpha = 5-8$. The streaming part is written as:

$$f_\alpha\left(\boldsymbol{x} + \boldsymbol{e}_\alpha\Delta t, t+\Delta t\right) = f_\alpha^+(\boldsymbol{x},t) \tag{6}$$

where the particles in location $\boldsymbol{x}$ at time t are streamed to location $(\boldsymbol{x}+\boldsymbol{e}_\alpha\Delta t)$ at time $(t+\Delta t)$. To end up the streaming process, by using moments of the discrete-velocity distribution functions, the macroscopic variables (ρ, p and $\boldsymbol{u}$) are evaluated as

$$\rho = \sum_\alpha f_\alpha(\boldsymbol{x},t), \quad \boldsymbol{u} = \frac{1}{\rho}\sum_\alpha \boldsymbol{e}_\alpha f_\alpha(\boldsymbol{x},t), \quad p = c_s^2\rho \tag{7}$$

where coordinate $\boldsymbol{x} \in R^2$, velocity field $\boldsymbol{u} \in R^2$, time $t \in R^+$, pressure $p \in R^2$, fluid density $\rho \in R^+$, kinematic viscosity $\nu \in R^+$. The dimensionless flow variables are expressed as $\boldsymbol{x}^* = \boldsymbol{x}/D$, $\boldsymbol{u}^* = \boldsymbol{u}/U_\infty$, $t^* = tU_\infty/D$, $p^* = (p - p_0)/(\rho U_\infty^2)$, and $Re = DU_\infty/\nu$, $M = U_\infty/c_s$, where U_∞, D, ν, and p_0 stands for reference velocity, reference length, kinematic viscosity and reference pressure, respectively.

2.1.1 Multiple-relaxation-time lattice Boltzmann

In order to improve the stability of single relaxation time approach, the multiple-relaxation-time approach is applied.[52] The method provides individual frequencies of collision for the various moments. Accordingly, the single relaxation time term in the equation (4) is replaced with the multiple-relaxation-time matrix to obtain the multiple-relaxation-time-Bhatnagar-Gross-Krook equation as

$$f_\alpha^+(\boldsymbol{x}, t) = f_\alpha(\boldsymbol{x}, t) - \boldsymbol{M}^{-1}\boldsymbol{S}\boldsymbol{M}\left(f_\alpha(\boldsymbol{x}, t) - f_\alpha^{eq}(\boldsymbol{x}, t)\right)\Delta t \tag{8}$$

where $\boldsymbol{M}$ is the 9×9 transformation matrix, which is written as

$$\boldsymbol{M} = \begin{pmatrix} 1 & 1 & 1 & 1 & 1 & 1 & 1 & 1 & 1 \\ -4 & -1 & -1 & -1 & -1 & 2 & 2 & 2 & 2 \\ 4 & -2 & -2 & -2 & -2 & 1 & 1 & 1 & 1 \\ 0 & 1 & 0 & -1 & 0 & 1 & -1 & -1 & 1 \\ 0 & -2 & 0 & 2 & 0 & 1 & -1 & -1 & 1 \\ 0 & 0 & 1 & 0 & -1 & 1 & 1 & -1 & -1 \\ 0 & 0 & -2 & 0 & 2 & 1 & 1 & -1 & -1 \\ 0 & 1 & -1 & 1 & -1 & 0 & 0 & 0 & 0 \\ 0 & 0 & 0 & 0 & 0 & 1 & -1 & 1 & -1 \end{pmatrix} \tag{9}$$

The collision matrix $\boldsymbol{S}$ is diagonal in a moment space and written as

$$\boldsymbol{S} = diag\left(s_0, s_1, s_2, s_3, s_4, s_5, s_6, s_7, s_8\right) \tag{10}$$

where $s_0 = s_3 = s_5 = 1.0$, $s_1 = s_2 = 1.4$, $s_4 = s_6 = 1.2$, and $s_7 = s_8 = 1/\tau$, where τ is related to the physical kinematic viscosity of the fluid (ν_0) by the following equation

$$\nu_0 = c_s^2\left(\tau - \frac{1}{2}\right)\Delta t \tag{11}$$

2.1.2 Blocked-structured parallel topology-confined mesh refinement

The framework of the present mesh generation is developed based on the framework of Uchibori and Tamura,[53] which is based on CUBE.[54] The computational domain is discretized by using uniform-spacing Cartesian mesh called blocks. The blocks are subdivided into child blocks of smaller size confined in the interest regions, such as around a solid body. As a result, the set of blocks is generated with the block level l ranging from coarsest level ($l = 0$) to finest level ($l = m-1$), where m is the total number of levels and $m-1$ is the number of refinements. In each block, the identical cells are distributed for easy partitioning, producing blocks with independent and identical workloads for parallelization. The efficient data structure is applied to store these blocks into linear arrays of coordinates, size, index, cell number, and index of neighbouring block, thus allowing scalability. The example of block-structured topology-confined mesh refinement is shown in Fig. 1a-c. The upper-half and lower-half domains show the block structure and subdivision of block into cells, respectively. The present block structure is parallelized by a combination of MPI and OpenMP approaches. The independent blocks are divided between MPI ranks; while the OpenMP thread parallelization is carried out for the numerical algorithm of a per-block basis. For the MPI partitioning, the load-balanced linear distribution based on a space-filling curve is employed.[55]

The computational procedure for the time advancement used in block structure is based on the work of Rohde et al.[56] As shown in Fig. 1d, two refinement levels (l - coarse level, $l+1$ - fine level) are sampled. While the original collision-streaming step is performed during Δt at the coarse level, it is performed during $0.5\Delta t$ at the fine level. This step is added by the explosion and coalescence operations. In the former operation, the information of the coarse level is transferred to the fine level after the first collision step at $0.5\Delta t$. In the latter operation, the information of the fine level is passed back to the coarse level at Δt.

To find the solution of each target block, the halo cells surrounding this block must be filled out. The halo cells are the additional layers of cells, which span across into the neighbouring blocks to enable the collision-streaming step at the block edges. As shown in Fig. 1e, the halo cells are distributed into three interfaces: coarse-fine, fine-fine, and fine-coarse. In the fine-fine interface, the boundary interior cells of the neighbouring blocks adjoin the halo cells; the information of boundary interior cells is copied into the halo cells of target block. In the coarse-fine interface, boundary interior cells of the coarser block are split into child cells, which adjoin the hallo cells of the target block (the explosion in Fig. 1d). In the fine-coarse interface, the information is copied from the halo cell centers of the finer block into those of the target block (the coalescence in Fig. 1d). All the information exchange is based on the MPI operation.

2.1.3 Interpolated bounce-back boundary condition

In LBM, the boundary conditions are clearly identified in terms of distribution functions (f_α). Otherwise, in the case of wall-bounded flows, the difficulty of LBM arises as the boundary conditions for f_α are not specified. In order to deal with the issue, the particle reflection approach, named as simple bounce-back method of first-order accuracy is utilized.[57] However, two error sources were found relating to staircase discretization and artificial slip velocity due to the usage of relaxation rate. To eliminate those error sources, Bouzidi et al.[58] proposed the interpolated bounce-back method of second-order accuracy, at which the additional constraint was introduced about the wall location. The intersection of a boundary link ($\boldsymbol{e}_\alpha$) and the solid boundary is generally at $\boldsymbol{x}_w$. Three lattice cell centers were respectively introduced by nearest fluid cells to the boundary surface ($\boldsymbol{x}_f$), solid cells ($\boldsymbol{x}_b = \boldsymbol{x}_f + \boldsymbol{e}_\alpha \Delta t$), and the fluid cells ($\boldsymbol{x}_{ff} = \boldsymbol{x}_f - \boldsymbol{e}_\alpha \Delta t$), as clearly shown in Fig. 1f.

In the interpolated bounce-back method, a linear interpolation is proposed to compute the a priori unknown bounced back distribution functions $f_{\bar{\alpha}}(\boldsymbol{x}_f, t+\Delta t)$ from the known post-collision distribution functions at $\boldsymbol{x}_f$ ($f_\alpha^+(\boldsymbol{x}_f, t)$) and $\boldsymbol{x}_{ff}$ ($f_\alpha^+(\boldsymbol{x}_{ff}, t)$)

$$f_{\bar{\alpha}}(\boldsymbol{x}_f, t+\Delta t) = \begin{cases} 2q f_\alpha^+(\boldsymbol{x}_f, t) + (1-2q) f_\alpha^+(\boldsymbol{x}_{ff}, t), & q \le \frac{1}{2} \\ \frac{1}{2q} f_\alpha^+(\boldsymbol{x}_f, t) + \frac{2q-1}{2q} f_{\bar{\alpha}}^+(\boldsymbol{x}_f, t), & q \ge \frac{1}{2} \end{cases} \tag{12}$$

where q is the ratio of the distance between $\boldsymbol{x}_f$ and $\boldsymbol{x}_w$ to the distance between $\boldsymbol{x}_f$ and $\boldsymbol{x}_b$

$$q = \frac{|\boldsymbol{x}_f - \boldsymbol{x}_w|}{|\boldsymbol{x}_f - \boldsymbol{x}_b|} \tag{13}$$

For curved boundaries, q varies and depends on the location of $\boldsymbol{x}_f$ and the lattice velocity $\boldsymbol{e}_\alpha$. As derived from equation (12), when q is equal to $1/2$, the distribution function of interpolated bounce-back method becomes that of simple bounce-back method.

2.1.4 Evaluations of force, hydrodynamic coefficients and time-averaged field

As established by Yu et al.,[59] the total fluid force ($\boldsymbol{F}(F_x, F_y)$, where F_x and F_y are the streamwise and transverse components of the total fluid force acting on the solid boundary, respectively) is written as

$$\boldsymbol{F}(F_x, F_y) = \sum_{\text{all }(\boldsymbol{x}_f)} \sum_{\alpha=1}^{N_Q} \boldsymbol{e}_{\bar{\alpha}} \left[f_\alpha^+ (\boldsymbol{x}_f, t) + f_{\bar{\alpha}}^+ (\boldsymbol{x}_f + \boldsymbol{e}_{\bar{\alpha}} \Delta t, t) \right] \left[1 - w(\boldsymbol{x}_f + \boldsymbol{e}_{\bar{\alpha}}) \right] \frac{\Delta x}{\Delta t} \tag{14}$$

where $N_Q = 8$ is the number of non-zero lattice velocity vectors and $w(\boldsymbol{x}_f + \boldsymbol{e}_{\bar{\alpha}})$ is an indicator, which is set as 0 at $\boldsymbol{x}_b$ and 1 at $\boldsymbol{x}_f$. The inner summation accounts for the momentum exchange between the nearest fluid cell ($\boldsymbol{x}_f$) and all possible neighbouring solid cells ($\boldsymbol{x}_b$). The outer summation computes the force contributed by all $\boldsymbol{x}_f$. The global hydrodynamic coefficients, such as lift and drag coefficients, pressure coefficient, Strouhal number, mean drag coefficient, and root-mean-square value of lift coefficient are accordingly computed as:

$$C_D = \frac{F_x}{\frac{1}{2}\rho U_\infty^2 D}, \quad C_L = \frac{F_y}{\frac{1}{2}\rho U_\infty^2 D}, \quad C_P = \frac{p - p_\infty}{\frac{1}{2}\rho U_\infty^2}, \quad St = \frac{f \cdot D}{U_\infty} \tag{15}$$

$$\overline{C}_D = \frac{1}{N} \sum_1^N C_D, \quad C_L' = \sqrt{\frac{1}{N} \sum_1^N \left(C_L - \overline{C}_L \right)^2} \tag{16}$$

The time-averaged normalized streamwise and transverse velocity, root-mean-squared normalized streamwise and transverse velocity, and time-averaged normalized Reynolds stress field are respectively computed as

$$u_{avg}^* = \frac{1}{U_\infty} \frac{1}{N} \sum_1^N u, \quad v_{avg}^* = \frac{1}{U_\infty} \frac{1}{N} \sum_1^N v \tag{17}$$

$$u_{rms}^* = \frac{1}{U_\infty} \sqrt{\frac{1}{N} \sum_1^N (u - u_{avg})^2}, \quad v_{rms}^* = \frac{1}{U_\infty} \sqrt{\frac{1}{N} \sum_1^N (v - v_{avg})^2} \tag{18}$$

$$\overline{u'v'} = \frac{1}{U_\infty^2} \frac{1}{N} \sum_1^N \left[(u - u_{avg}) (v - v_{avg}) \right] \tag{19}$$

where N is the number of instants of a time history data.

3 Computational setup

Fig. 2 shows flow configuration with computational domain and boundary conditions at the inlet, outlet, upper, and lower boundaries. As reported by Shi et al.,[43] the wake structures with multiple vortex shedding topologies (primary and secondary) are fully developed and detected behind the elliptic cylinder at the inclination angle of 90^0 and the aspect ratio of 0.5. To capture the underlying vortex dynamics in this paper, the major axis (D) and the aspect ratio of three elliptic cylinders are set the same. The upstream cylinder (referred to as E1 hereafter) is located at the coordinate origin;

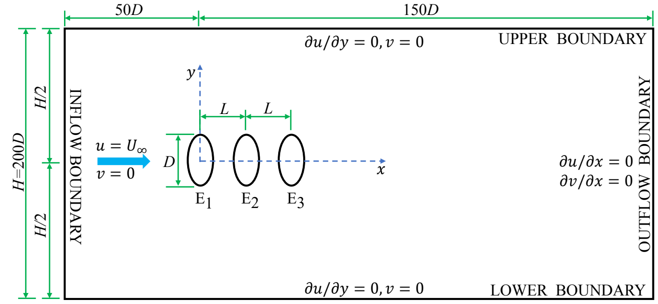

Figure 2: Flow configuration with computational domain and boundary conditions at inlet, outlet, upper, and lower boundaries. The major axis of elliptic cylinder is located at 90^0. The aspect ratio of elliptic cylinder is 0.5.

Table 1: Comparison of flow past a single circular cylinder at Re=50, 100, 150, and 200

Re	Authors	$\overline{C}_D$	C'_L	St
	Qu et al.[61]	1.397	0.039	0.124
$Re = 50$	Chen et al.[62]	1.427	0.039	0.123
	Present	1.426	0.039	0.127
	Williamson[63]	–	–	0.164
	Chen et al.[62]	1.337	0.230	0.163
$Re = 100$	Present	1.335	0.221	0.168
	Qu et al.[61]	1.306	0.355	0.184
$Re = 150$	Chen et al.[62]	1.316	0.363	0.181
	Present	1.316	0.359	0.188
	Qu et al.[61]	1.320	0.457	0.196
$Re = 200$	Chen et al.[62]	1.324	0.474	0.194
	Present	1.325	0.475	0.201

while the positions of the middle cylinder (E2) and downstream cylinder (E3) are simultaneously changed to ensure the identical spacing (L) between them. The spacing ratios (L/D) range from 1.5 to 10 with an increment of 0.5. The domain of computation is $200D \times 200D$ so that the blockage ratio ($B = D/H$, where H is the width of the computational domain) is 0.5%, which is less than the required blockage ratio threshold of 6%.[60] For the setup of boundary conditions shown, the Dirichlet-type and Neumann-type boundary conditions are adopted for the inflow and the outflow boundaries, respectively; while the upper and lower boundaries are set as free-slip. To capture fully developed vortex shedding patterns, the 2D simulations are conducted for non-dimensional time $t^* > 3000$, after the asymptotic wake state has been reached.

In this paper, the numerical algorithm is validated for a single circular cylinder at $Re = 50 - 200$ (table 1), two side-by-side circular cylinders at $L/D = 2.5$ and $Re = 100$ (table 2), three tandem circular cylinders at $L/D = 5$ and $Re = 160$ (table 3), and single elliptic cylinder at $AR = 0.5$, $\gamma = 90^0$, and $Re = 150$ (table 4), where the hydrodynamics coefficients ($\overline{C}_D$, C'_L) and Strouhal number (St)

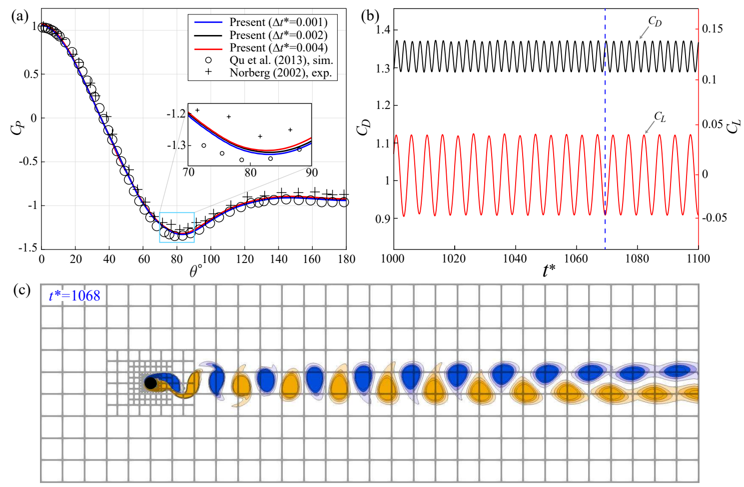

Figure 3: Comparison of pressure coefficients distributions along the cylinder surface at $Re = 200$ between the reported experimental and numerical data and the present data (a); The time history of lift and drag coefficients (b); The instantaneous vorticity field at $t^* = 1068$ with the block-structured topology-confined mesh distribution (c)

are calculated and compared with those listed in the literature. In table 1, the maximum deviation between the results is small, indicating a good agreement of the present numerical algorithm for the range of Re inspected. In Fig. 3, the block level and cells are selected as 5 and 40^2, respectively. The temporal convergence study is performed with three different time steps ($\Delta t^* = 0.001$, 0.002, and 0.004); and the present results of time-mean surface pressure coefficient collapse the reference results.[61,64] Hence, the non-dimensional time step of 0.002 is chosen for subsequent simulations. In table 2, the present results at $B = 0.005$ agrees well with those in Chen et al.[62] and Bao, Zhou and Tu;[65] while at $B = 0.02$ the large difference of St (19.5%) is observed between the present result and that of Lee et al.[66] Therefore, a blockage ratio of 0.005 is adopted. The same time step, blockage ratio, and number of refinement levels and cells are applied for the simulations of flow past three tandem circular cylinders (table 3) and a single elliptic cylinder (table 4); and the results are compared with the references. As shown in these tables, the present results are in good agreement with the reference results. In table 5, the performance of meshes is conducted for spatial convergence study to choose a fairly good grid resolution by selecting block level and cells. Four meshes of M1, M2, M3, and M4 with selected block level and cells are performed corresponding to $y^+ = 0.117$, 0.1, 0.085, and 0.0625, respectively. The error norm is computed based on the results of the M4 mesh. At M3 mesh, the results of E1 and E2 are less than 1%; while the results of E3 are maximum at 3.1%. Thus, it is fair to adopt M3 mesh.

4 Spacing ratio effects

Based on the visualization technique presented by zdravkovich,[13,19,68] three distinct flow regimes are identified for the flow past two tandem circular cylinders. These flow regimes were named as overshoot

Table 2: Comparison of flow past a side-by-side circular cylinders at $L/D = 2.5$ and Re=100

Authors	$\overline{C}_D$	C'_L	St
Chen et al.[62]($B = 0.005$)	1.424	0.176	0.191
Bao, Zhou and Tu[65]($B = 0.005$)	1.431	0.177	0.211
Lee et al.[66]($B = 0.02$)	1.423	0.178	0.169
Present($B = 0.005$)	1.429	0.175	0.198
Present($B = 0.02$)	1.443	0.179	0.202

Table 3: Time-mean drag coefficient ($\overline{C}_D$), root-mean-square value of lift coefficient (C'_L) and Strouhal number (St) of three tandem circular cylinders at $L/D = 5.0$ and $Re = 160$

	Cylinder 1			Cylinder 2			Cylinder 3		
	$\overline{C}_D$	C'_L	St	$\overline{C}_D$	C'_L	St	$\overline{C}_D$	C'_L	St
Present	1.290	0.931	0.175	0.420	0.392	0.175	0.158	0.271	0.175
Zhu et al.[35]	1.287	0.922	0.171	0.411	0.385	0.171	0.151	0.264	0.171
Error (%)	0.23	0.98	2.3	2.2	1.8	2.3	4.6	2.6	2.3

Table 4: Comparison of the results for single elliptic cylinder at $AR = 0.5$, $\gamma = 90^0$, and $Re = 150$

Authors	$\overline{C}_D$	St
Present	1.837	0.193
Shi et al.[43]	1.824	0.191
Thompson et al.[67]	1.78	0.189

Table 5: Mesh independence results for three tandem elliptic cylinders at $AR = 0.5$, $\gamma = 90^0$, $L/D = 5.0$ and $Re = 100$

Mesh		M1	M2	M3	M4
block level/cells		$5/34^2$	$5/40^2$	$6/12^2$	$6/16^2$
y^+		0.117	0.1	0.085	0.0625
E1	$\overline{C}_D$	1.7689 (1.16%)	1.7742 (0.86%)	1.7834 (0.34%)	1.7896
	C'_L	0.4213 (5.60%)	0.4376 (1.94%)	0.4437 (0.58%)	0.4463
	St	0.171 (2.28%)	0.174 (0.57%)	0.175 (0%)	0.175
E2	$\overline{C}_D$	0.4175 (3.93%)	0.4101 (2.09%)	0.4052 (0.87%)	0.4017
	C'_L	0.5645 (4.09%)	0.5522 (1.82%)	0.5462 (0.72%)	0.5423
	St	0.179 (2.28%)	0.177 (1.14%)	0.176 (0.57%)	0.175
E3	$\overline{C}_D$	0.0831 (4.15%)	0.0843 (2.76%)	0.0861 (0.69%)	0.0867
	C'_L	0.1168 (7.44%)	0.1197 (5.15%)	0.1224 (3.1%)	0.1262
	St	0.170 (2.85%)	0.171 (2.28%)	0.173 (1.14%)	0.175

($1.0 < L/D < 2.0$), reattachment ($2.0 < L/D < 3.5$), and co-shedding ($L/D > 3.5$). In the co-shedding regime, while the upstream cylinder always exhibits primary vortex shedding mode, two-layered and secondary vortex shedding modes are observed behind the middle cylinder for $3.5 < L/D < 6.5$ and $6.5 < L/D < 10.0$, respectively.[35] The first and third modes show staggered counterrotating vortices; while the second mode presents two parallel vortex layers, where each layer is distributed by detectable individual vortices of the same sign. In this section, the flow characteristics of three tandem elliptic cylinders are discussed at the range of $L/D = 1.0 - 10.0$ and $Re = 100$. Fig. 4 − 7 illustrate wake interference at representative spacing ratios of $L/D = 1.5$, 3.0, 5.0, and 9.5, respectively. In each figure, the instantaneous lift coefficients of individual cylinders and their associated frequencies (St) are displayed. A sequence of instantaneous normalized vorticity contours ($\omega_z^* = \omega_z D/U_\infty$) in a shedding cycle of E1 or E3 is also presented. The contours of root-mean-squared and time-averaged normalized streamwise velocities are shown with the time-averaging interval of 1000 time units. The wake structures are classified into four regimes: overshoot ($1.5 \leq L/D \leq 2.0$), reattachment ($2.0 < L/D \leq 3.0$), quasi-coshedding ($3.0 < L/D < 8.5$), and coshedding ($8.5 \leq L/D \leq 10.0$). The details of these regimes are produced in the following subsections.

4.1 Classification of flow regimes

4.1.1 Overshoot regime ($1.5 \leq L/D \leq 2.0$)

For small L/D, the lower and upper shear layers from E1 overshoot E2 and E3, introducing the stagnant flows between these cylinders as shown at moment i of Fig. 4b. These shear layers cross-annihilate each other behind E3, raising the nonlinearity of the flow. As a result, the clockwise vortex grows its strength and starts to roll up at approximately $4.5D$ behind E3, signifying the maximum peak of C_L of E3. At moment ii, the clockwise vortex (labeled B) cuts off from the shear layer at $7D$ downstream, leading to the sufficiently small C_L of E3. At moments iii and iv, the vortex B convects downstream in the primary vortex shedding mode, signifying the identical frequencies of C_L of three cylinders. The peaks of C_L of E3, E2, and E1 gradually reduce, indicating the proximity effect of these cylinders. The formation and convection of the anti-clockwise vortex (labeled A) at moments i and ii are similar to those of the clockwise vortex (labeled F) at moments iii and iv in opposite direction. Furthermore, the contour of u^*_{rms} clearly shows the signatures of the shear layers on the C_L of E2 and E3 in overshoot regime. The values of u^*_{rms} near top and bottom sides of E3 are higher than those of E2, making the peak of C_L of E3 larger than that of E2. The contour of u^*_{rms} shows the single-bluff body flow regime, at which the length (L_E) and width (W_E) of the recirculation zone are approximately $1.5D$ streamwise and $1.1D$ transverse distances from E3, respectively.

4.1.2 Reattachment regime ($2.0 < L/D \leq 3.0$)

With the increase in L/D, the reattachment flow regime is observed in Fig. 5. At moment i, the clockwise vortex (labeled B) breaks up with the shear layer from the top of E1. Simultaneously, the counterclockwise vortex (labeled A) grows into the maximum size from the bottom of E1, thus forming the primary vortex shedding mode behind the E1. Vortex B reattaches to the top of E2 and amalgamates with the same sign vortex shed from E2, introducing the associated vortex that signifies the higher peak of C_L of E2 than that of E1. At moment ii, the vortex B convects toward E3 in the same mode. At moment iii, the vortex B rolls up the top of E3. At moment iv, the vortex B

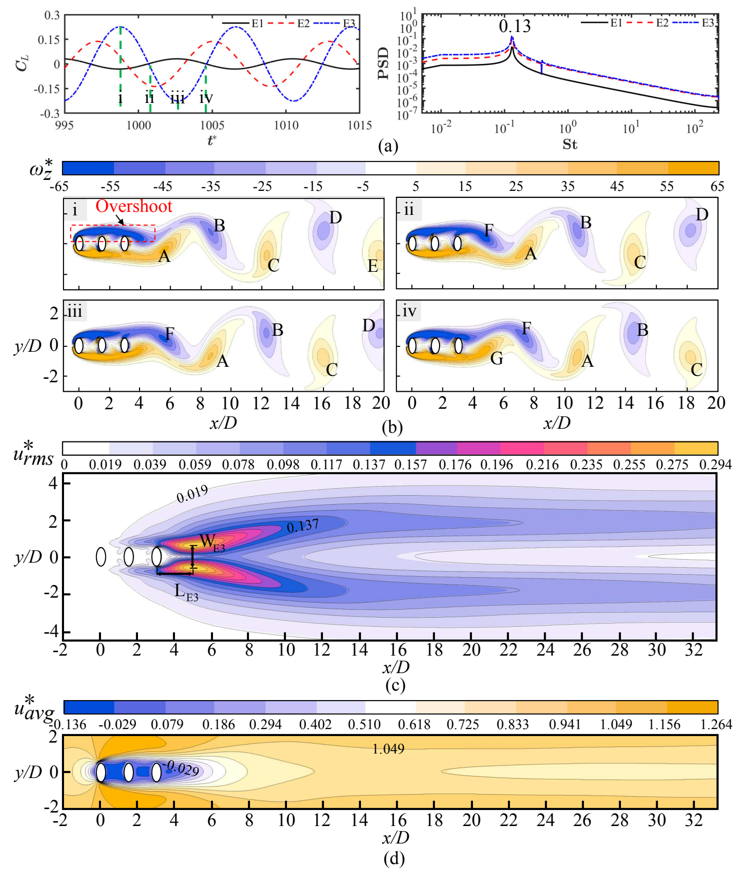

Figure 4: Flow characteristics for $Re = 100$ and $L/D = 1.5$. (a) instantaneous lift coefficient and associated frequency spectra with the time interval consisting of more than 200 near wake shedding cycles of E3, (b) a sequence of instantaneous vorticity fields in a shedding cycle, (c) contour of root-mean-square streamwise velocity, (d) contour of time-averaged streamwise velocity

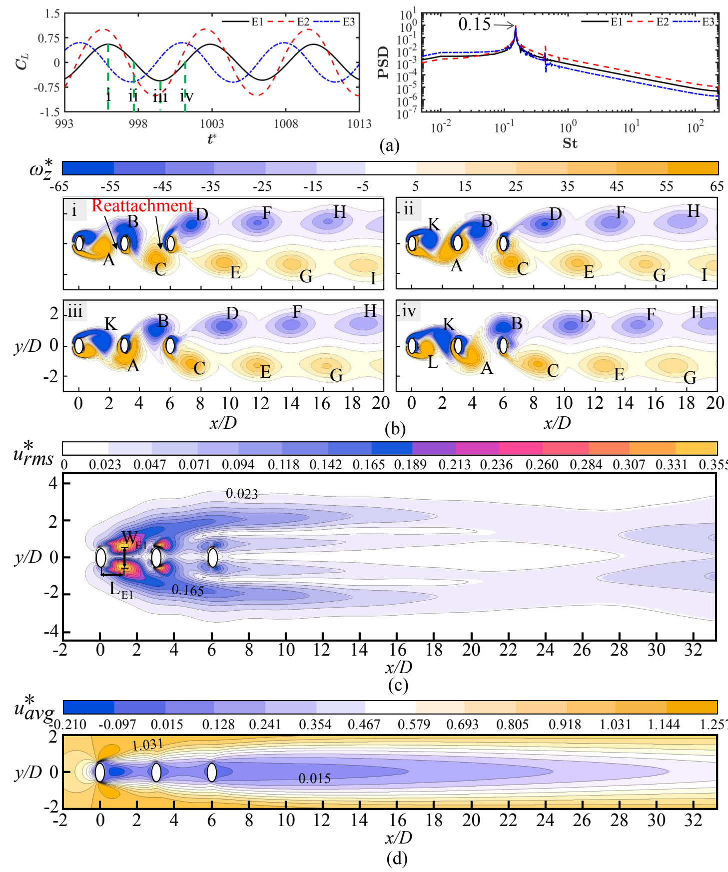

Figure 5: Flow characteristics for $Re = 100$ and $L/D = 3$. (a) instantaneous lift coefficient and associated frequency spectra with the time interval consisting of more than 200 near wake shedding cycles of E1, (b) a sequence of instantaneous vorticity fields in a shedding cycle, (c) contour of root-mean-square streamwise velocity, (d) contour of time-averaged streamwise velocity

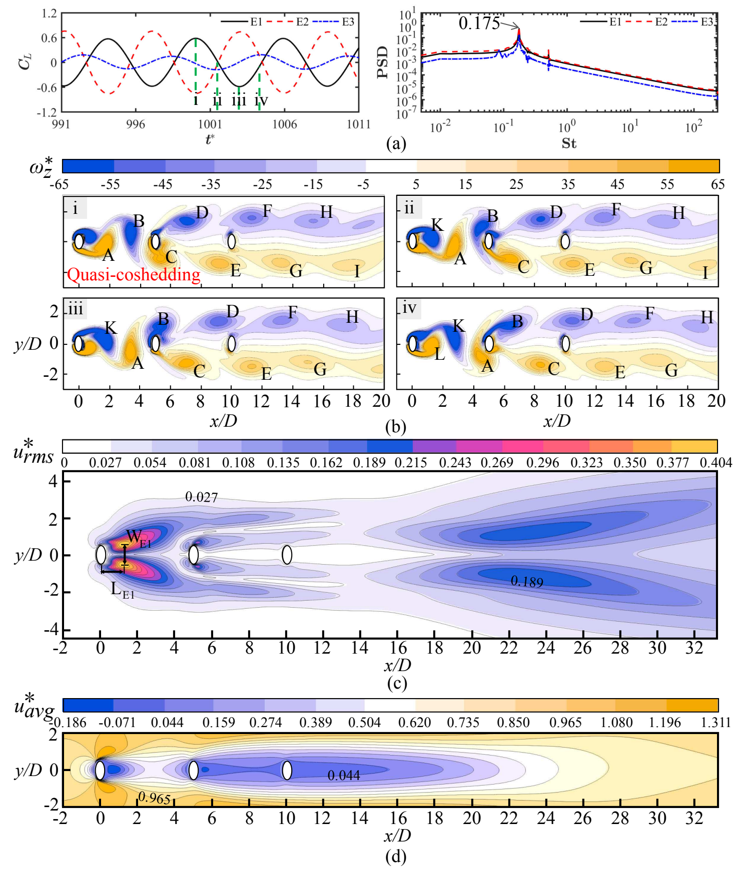

Figure 6: Flow characteristics for $Re = 100$ and $L/D = 5$. (a) instantaneous lift coefficient and associated frequency spectra with the time interval consisting of more than 200 near wake shedding cycles of E1, (b) a sequence of instantaneous vorticity fields in a shedding cycle, (c) contour of root-mean-square streamwise velocity, (d) contour of time-averaged streamwise velocity

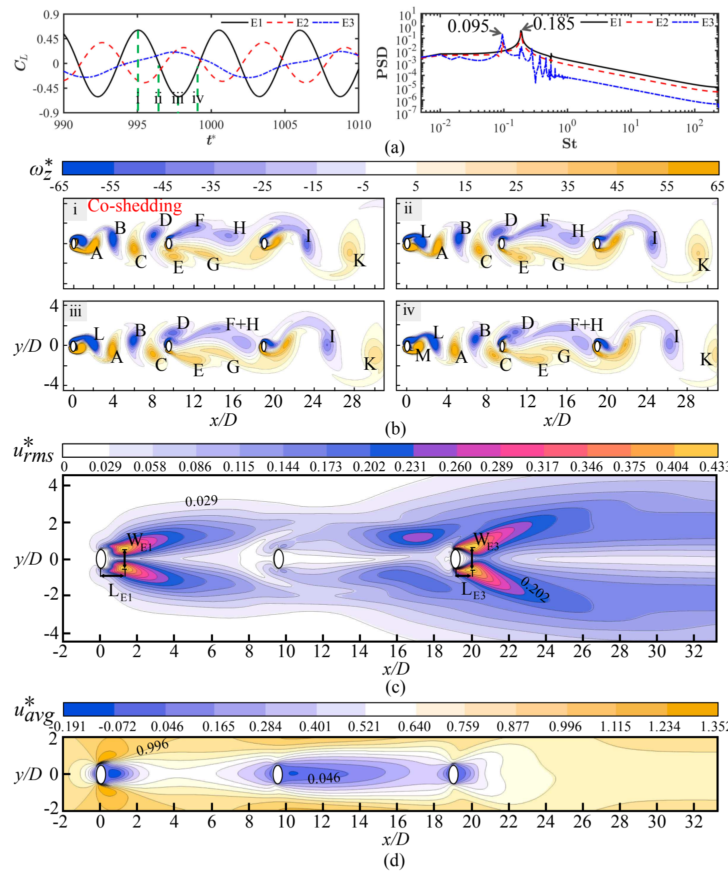

Figure 7: Flow characteristics for $Re = 100$ and $L/D = 9.5$. (a) instantaneous lift coefficient and associated frequency spectra with the time interval consisting of more than 200 near wake shedding cycles of E1, (b) a sequence of instantaneous vorticity fields in a shedding cycle, (c) contour of root-mean-square streamwise velocity, (d) contour of time-averaged streamwise velocity

amalgamates with the same sign vortex shed from E3, generating the associated vortex that convects downstream in two-layered vortex shedding mode. Specifically, the detectable individual clockwise and counterclockwise vortices are aligned in upper and lower layers, respectively. The peak of C_L of E2 is larger than that of E3, indicating the stronger impingement of vortex B on E2 than that on E3. The boundary separating these two modes is located at approximately $6D$ downstream. The formation and convection of counterclockwise vortices A and C at moments iii and iv are similar to those of clockwise vortices B and D at moments i and ii in opposite direction. The primary vortex shedding mode dominates three cylinders, showing their low identical frequencies of C_L ($St = 0.15$). However, due to the vortex amalgamations, the frequency of three elliptic cylinders is less than that of a single one ($St = 0.19$ obtained by Thompson et al.[67]). In the contour of u^*_{rms}, the primary vortex shedding mode signifies strong vortex bubbles behind E1 and E2; while the two-layered vortex shedding mode induces slightly weaker vortex bubbles behind E3. In the two-layered vortex shedding mode, the flow is symmetric from approximately $5D$ to $21D$ downstream. Otherwise, secondary vortex shedding mode with the distribution of long streamwise wavelength vortices occurs from $21D$ downstream, behaving the asymmetric flow (as expressed in subsection 4.2). Furthermore, the width of recirculation zone behind E2 is wider than that of E1, thus explaining the larger peak of C_L of E2 than that of E1.

4.1.3 Quasi-coshedding regime ($3.0 < L/D < 8.5$)

For $3.0 < L/D < 8.5$, the wake flow transforms into quasi-coshedding regime, at which the primary vortex shedding mode occurs behind E1 and two-layered vortex shedding mode occurs behind E2 and E3 (Fig. 6). The vortex amalgamation occurs only on the top and bottom of E2 (Fig. 6b). After the amalgamation, the clockwise vortex (labeled B) convects, rolls up, and passes through the top of E3 in the two-layered vortex shedding mode that ranges from approximately $5D$ to $14D$ downstream. Due to this vortex amalgamation, the phase lag of C_L of E2 is larger than that of E3. The vortex amalgamation also makes the peak of C_L of E2 higher than that of E1 and E3. As shown in frequency spectra, the identical frequencies of C_L are observed as 0.175, indicating the dominant frequency of the primary vortex shedding mode. In comparison with other flow regimes, the dominant frequency of C_L in quasi-coshedding regime is higher than that in overshoot and reattachment regimes; and due to the large interference effect, it is smaller than that of single cylinder ($St = 0.19$). In the contour of u^*_{rms}, the symmetric vortex bubbles behind three cylinders are obtained, thus ensuring the sufficient time-averaging interval. In addition, the two-layered vortex shedding mode switches to the secondary vortex shedding mode at approximately $23.1D$ downstream, which will be presented in more detail in subsection 4.2. The primary vortex shedding mode signifies strong vortex bubbles behind E1; while the vortex amalgamation introduces weak vortex bubbles behind E2.

4.1.4 Coshedding regime ($8.5 \leq L/D \leq 10.0$)

For $8.5 \leq L/D \leq 10.0$, the fully developed coshedding flow regime is observed, at which the vortex sheddings are simultaneously evolved behind three elliptic cylinders (Fig. 7). Two frequency peaks of C_L are observed corresponding to secondary vortex shedding mode behind E3 ($St = 0.095$) and primary vortex shedding mode behind E1 ($St = 0.185$). At moment i, the clockwise vortex (labeled D) transports in the primary vortex shedding mode. At moment ii, the vortex D rolls up the frontal surface of E2. At moment iii, this vortex starts to amalgamate with the same sign vortex shed from

E2 to form associated vortex behind E2. The clockwise vortices (labeled F and H) are the parent and grandparent of the vortex D, respectively. After shedding from E2, they convect, interact, and merge into a strongly weighted vortex (labeled F+H) before evolving reattachment to the frontal surface of E3, as seen in moments ii, iii, and iv. The clockwise vortex (labeled I) shed from E3 at the moment i is the parent of vortex F+H after reattaching and amalgamating with the same sign vortex shed from E3. Hence, the vortex I formed by the second amalgamation has higher strength than the vortex F formed by the first amalgamation. As a result, the maximum values of u^*_{rms} behind E3 is larger than that behind E2. In addition, due to the roll-up of vortex D on E2 and reattachment of vortex F+H to frontal surfaces of E3, the peaks of C_L of E2 and E3 are smaller than the peak of C_L of E1. Furthermore, the frequency of C_L of E1 ($St = 0.185$) approaches that of single elliptic cylinder ($St = 0.19$), indicating the weak interference effect of E2 and E3 on E1. In the field of u^*_{rms}, the length of recirculation zone behind E3 is larger than that behind E1, suggesting the longer streamwise wavelength vortices in secondary vortex shedding mode than those in primary vortex shedding mode. Since the vortex F+H undergoes aperiodic motion, two asymmetric vortex bubbles in front of E3 are observed.

4.2 Flow characteristics

Because the overshoot regime is identical with single bluff-body flow, in this section flow characteristics of three distinct flow regimes: reattachment, quasi-coshedding, and coshedding are presented in Fig. 8 at four representative spacing ratios, including $L/D = 3.0, 5.0, 8.5$, and 9.0. At each L/D, instantaneous normalized vorticity field, time-averaged normalized streamwise and transverse velocity fields, and normalized Reynolds stress are orderly displayed from top to bottom. The instantaneous normalized vorticity field is sampled at a non-dimensional time instant $t^* = 2100$, where the wake flow is fully developed into three distinct vortex shedding modes: primary, two-layered, and secondary. Boundaries separating vortex shedding modes are marked by vertical dashed lines. The black vertical dashed line is the near wake transition from primary vortex shedding mode to two-layered vortex shedding mode (referred to as the first boundary hereafter). The red vertical dashed line is the intermediate wake transition from two-layered vortex shedding mode to secondary vortex shedding mode (referred to as the second boundary hereafter). All the time-averaged contours are generally symmetric about the cylinder centerline, indicating the sufficiently averaging time.

As shown in the field of v^*_{avg}, the first boundaries are determined by the first local maximum based on the v^*_{avg} values, including the first local positive maximum of v^*_{avg} above the cylinder centerline and the first local negative maximum of v^*_{avg} below the cylinder centerline. On the first boundaries, the vortices divert from the cylinder centerline and follow two offset layers (presented in the field of ω^*_z). Otherwise, the second boundaries are determined by the second local maximum, where the vortices converge the cylinder centerline. The vorticity convergence marks the second local negative maximum above the cylinder centerline and the second local positive maximum below the cylinder centerline. Based on these local maxima, the range of two-layered vortex street are determined as $x/D = 5-35.3$, $x/D = 5.75-21.5$, $x/D = 8.0-20.1$ and $x/D = 8.5-19$ at $L/D = 3.0$, 6.0, 8.5 and 9.0, respectively. It is interesting to note that the range of two-layered vortex street is narrowing with an increase in L/D. The first boundary always appears near the frontal surface of E2, signifying the effect of middle cylinder on the switch from primary to two-layered vortex shedding modes. Furthermore, the second boundary gradually moves upstream with an increase in L/D. Otherwise, the intensively shearing flow

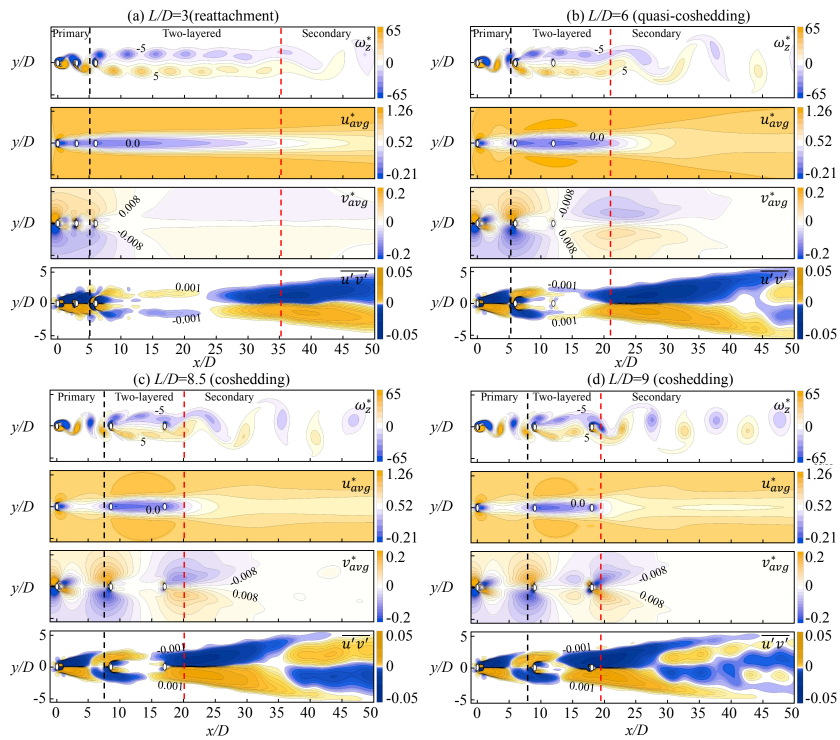

Figure 8: Flow characteristics for $Re = 100$: (a) $L/D = 3.0$; (b) $L/D = 6.0$; (c) $L/D = 8.5$; (d): $L/D = 9.0$. Boundaries separating vortex shedding modes are marked by vertical dashed lines. The black vertical dashed line is the boundary between primary and two-layered vortex shedding modes. The red vertical dashed line is the boundary between two-layered and secondary vortex shedding modes.

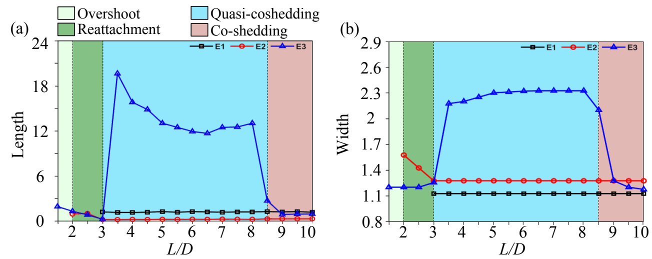

Figure 9: The variations of length (a) and width (b) of recirculation zones behind three elliptic cylinders with L/D at $Re = 100$

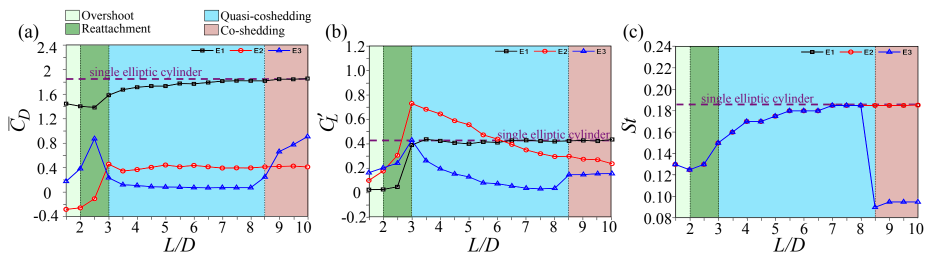

Figure 10: The variations of $\overline{C}_D$ (a), C_L' (b), and St (c) with L/D for three elliptic cylinders at $Re = 100$

regions are observed at two boundaries in the field of $\overline{u'v'}$; and the streamwise velocity bubble between the two boundaries indicates the signature of two-layered vortex shedding mode in the field of u^*_{avg}.

4.3 Vortex formation length and wake width

Fig. 9 shows variations of the length and width of vortex bubbles behind three elliptic cylinders at the range of $L/D = 1.5 - 10.0$. From $L/D = 3.0$ to 10.0, the vortex bubble length and width of E1 and E2 are small values. That is because at asymptotic wake state the primary and two-layer vortex shedding modes occur behind E1 and E2, respectively. When the flow transforms from reattachment to quasi-coshedding, the vortex bubble length and width of E3 dramatically jump at $L/D = 3.0-3.5$ due to the appearance of secondary vortex shedding mode in intermediate wake. The vortex bubble length of E3 gradually reduces at the range of $L/D = 3.5 - 6.5$, also suggesting that the second boundary (presented in Fig. 8) gradually moves upstream with the increase in L/D. In addition, the vortex bubble length and width of E3 show a sharp drop when the flow transforms from quasi-coshedding to fully developed coshedding regimes. It is because the two-layered vortex shedding mode behind E3 suddenly switches to secondary vortex shedding mode at sufficiently large L/D.

4.4 Hydrodynamic coefficients and Strouhal numbers

Fig. 10 depicts the variations of $\overline{C}_D$, C_L' and St with L/D. To highlight the proximity effect, these coefficients of three tandem elliptic cylinders are compared with those of the single elliptic cylinder obtained by Thompson et al.[67] The $\overline{C}_D$ of E1 are larger than those of E2 and E3 due to the shadowing effect, which is identical with the flow past three tandem circular cylinders.[35] Otherwise, $\overline{C}_D$ of E1 is below that of single elliptic cylinder due to the vortex-cylinder interference, where the E2 and E3 interfere the wake of E1, thus reducing the $\overline{C}_D$ of E1. For $1.5 \leq L/D \leq 2.0$, the stagnant flows in overshoot regime signify the tiny reduction of $\overline{C}_D$ of E1; while keeping significant increase in $\overline{C}_D$ of E3. The $\overline{C}_D$ of E2 is negative due to its sandwiched position between two stagnant flows. In addition, the C'_L of E1 is nearly zero; while the C'_L of E2 and E3 also show a tiny increase. For $2.0 < L/D \leq 3.0$, the $\overline{C}_D$ of E2 dramatically increases from negative to a positive value, signifying the drag inversion region. The $\overline{C}_D$ of E2 approaches the maximum value at $L/D = 3.0$, which is defined as the critical spacing ratio. This critical spacing ratio is smaller than that of three tandem circular cylinders ($L/D = 3.5$ observed by Zhu et al.[35]). At this critical spacing ratio, the values of C'_L of three cylinders also express a sharp jump as the reattachment transforms into quasi-coshedding. For $3.0 < L/D \leq 8.0$, the $\overline{C}_D$, C'_L, and St of E1 increase tinily; and they approach those of single circular cylinder at $L/D = 7.5$, suggesting small effect of E2 and E3 on E1. In addition, due to the vortex roll-up in the quasi-coshedding regime, the $\overline{C}_D$ of E3 are identically small as L/D increases. The C'_L of E2 is greater than that of E3 due to the vortex amalgamation described in reattachment, quasi-coshedding, and coshedding regimes. When L/D increases, the values of C'_L of E2 and E3 gradually decrease; while the values of $\overline{C}_D$ of the two cylinders vary slightly. The values of St of three cylinders are identical in the range of $L/D = 1.5 - 8.0$, indicating the dominant frequency of primary vortex shedding mode. For $8.5 \leq L/D \leq 10.0$, C'_L and $\overline{C}_D$ of E3 dramatically increase; while the St of E3 sharply drops, signifying the occurrence of secondary vortex shedding mode with low frequency in the intermediate wake.

5 Reynolds number effects

In the dynamics of flow around cluster of cylindrical structures, the Reynolds number always plays a crucial role. In this section, the effect of Reynolds number on the wake patterns, variation of time-mean centerline streamwise velocity, transition of vortex shedding modes, and flow irregularity are scrutinized. Three Reynolds numbers are considered as $Re = 65$, 100, and 160, which exceed the critical value ($Re = 47$) of periodic vortex shedding.[64] In addition, these low Reynolds numbers eliminate the turbulence caused by flow distortion, thus ensuring physically two-dimensional vortex dynamics.[50]

5.1 Wake patterns

As shown in Fig. 11, at $L/D = 1.5$, the single bluff-body flow is observed with occurrence of overshoot regime in asymptotic state of wake for both Reynolds numbers. At $L/D = 6.0$, alternating reattachment of vortex to the frontal surface of E2 is observed at $Re = 65$; while the vortex roll-up in front of E2 is observed at $Re = 160$. In the intermediate wake behind E3 at $L/D = 6.0$, while the meandering vortices are observed at $Re = 65$, the secondary vortex street is observed at $Re = 160$. That is because of the higher diffusivity of the flow at lower Reynolds numbers, where the vortex transports with the mean flow velocity. Furthermore, as shown in Fig. 11e, the stretched vortex at pairing intermittently and irregularly appears around the second boundary, where the paired vortices of the opposite sign cancel their strengths to form the weaker vortices. Hence, the irregularity of vorticity field occurs, which will be discussed in subsection 5.5. The observations of wake patterns at $L/D = 10.0$ for both

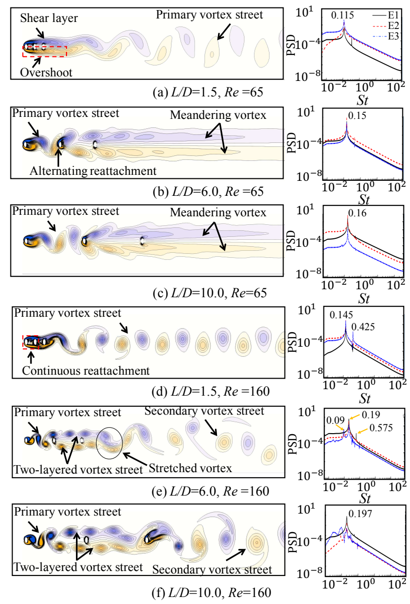

Figure 11: Asymptotic behavior of vorticity field (left) and lift coefficient spectra (right). (a)-(c) represent the results at $Re = 65$ and $L/D = 1.5$, 6, and 10.0, respectively. (d)-(f) represent the results at $Re = 160$ and $L/D = 1.5$, 6, and 10.0, respectively.

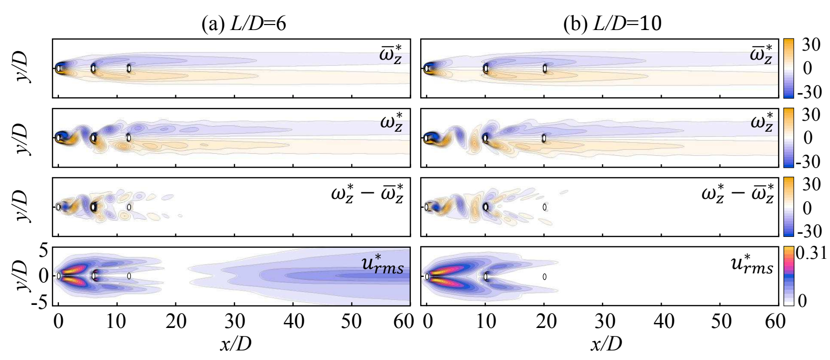

Figure 12: Meandering regime at $Re = 65$ for $L/D = 6.0$ (a) and $L/D = 10.0$ (b).

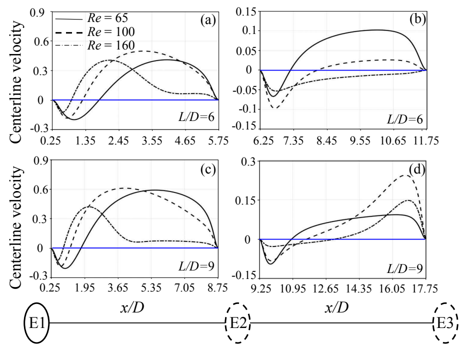

Figure 13: The variations of time-mean streamwise velocity profiles along the centerline with Reynolds numbers at $L/D = 6$ ((a) and (b)) and 10 ((c) and (d))

Reynolds numbers are identical with those at $L/D = 6.0$. As shown by the spectra of C_L of three cylinders, the dominant frequency of primary vortex shedding gradually rises with the increase in L/D for both Reynolds numbers. Otherwise, only primary vortex shedding frequency is observed at $Re = 65$ (Fig. 11b); while another frequency peak corresponding to existence of secondary vortex shedding mode in the intermediate wake is detected at $Re = 160$ (Fig. 11e). The frequency of the secondary vortex shedding ($St = 0.09$) is lower than the frequency of primary vortex shedding ($St = 0.19$). Consistently, the vortex wavelength in secondary vortex shedding mode is longer than that in the primary vortex shedding mode.

The detailed behaviors of the meandering flow region are shown in Fig. 12 with representative spacing ratios ($L/D = 6$ and 10). In this figure, the time-averaged normalized vorticity, instantaneous normalized vorticity at asymptotic wake state ($t^* = 2200$), instantaneous normalized vorticity fluctuation ($\omega'_z = \omega^*_z - \bar{\omega}^*_z$), and normalized root-mean-square streamwise velocity are orderly arranged from top to bottom. The contour of ω'_z is produced to quantify the onset location of vortices in vortex shedding modes; while the contour of u^*_{rms} is produced to highlight the effect of these vortices on the velocity fluctuations around three elliptic cylinders. As shown in the contour of ω^*_z, the vortices from E1 alternately roll up on the top and bottom sides of E2 in the primary vortex shedding mode, and transform into the meandering regime behind E2. In this regime, these vortices are diffusive and move downstream with the mean flow velocity, where the contours of ω^*_z are identical with those of $\bar{\omega}^*_z$. In addition, in comparison with the three tandem circular cylinders,[35] the detectable individual vortices are not observed downstream in the meandering regime due to the effect of vortex diffusion at lower Reynolds number. In the contours of ω'_z, the strong vortex impingement is observed at the frontal surface of E2 (causing the high PSD peaks shown in Fig. 11b and 11c); while it can be seen that there is no shedding from E3. As shown in the contours of u^*_{rms}, the vortices in the meandering regime signify its small fluctuation on top and bottom sides of E3 at $L/D = 6$; while there is no fluctuation on E3 at $L/D = 10$, indicating that almost no new vortices are generated from E3.

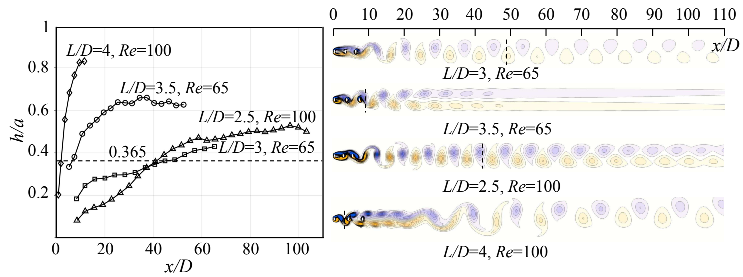

Figure 14: Left: variations of the vortex spacing ratios (h/a) with Re and L/D. Horizontal dashed line represents a vortex spacing ratio of 0.365. Right: associated wake structures. Vertical dashed lines correspond to the approximate position where $h/a = 0.365$

5.2 Variation of mean centreline velocity

Fig. 13 shows considerably different behaviors of mean streamwise velocity profiles at $Re = 65$, 100, and 160. As expressed in Fig. 13a and 13c, the negative streamwise velocity profiles signify the recirculation zones due to appearance of the primary vortex shedding mode behind E1 for three Reynolds numbers. At $Re = 160$, the regions, where the centerline streamwise velocity is approximately 8% of free stream velocity, correspond to the occurence of two-layered vortex shedding mode. The ranges of the regions are observed as $4.1 \leq x/D \leq 5.75$ at $L/D = 6.0$ and $4.1 \leq x/D \leq 8.25$ at $L/D = 9.0$. Apart from three tandem circular cylinder flow at $Re = 160$,[42] the formation of the first boundary for three tandem elliptic cylinders is independent with L/D. Fig. 13b shows the negative velocity profile at $Re = 160$, suggesting the reverse flow between E2 and E3 due to the domination of vortex convection at higher Reynolds numbers. However, the positive velocity profiles appear at $Re = 65$ because of the domination of vortex diffusion at lower Reynolds numbers; hence the vortices transport with the mean flow velocity. Fig. 13d shows the positive peaks of streamwise velocity profile at $Re = 100$ and 160, corresponding to the vortex reattachments to E3. The vortex reattachment at $Re = 100$ is stronger than that at $Re = 160$, suggesting the stronger vortex impingment on E3 at $Re = 100$ than that at $Re = 160$.

5.3 PVS–TVS transition

Karasudani and Funakoshi[69] scrutinized the stability of the topological vortices arranged in a wake. They pointed out that as the vortex spacing ratios (h/a, where a and h are the longitudinal distance of two vortex centers of opposite sign and transverse distance of two vortex centers of same sign, respectively) exceeds 0.365, the vortices of opposite sign would alternately roll up, diffuse and arrange in two parallel straight lines forming two-layered vortex street. To examine the near wake transition from primary vortex shedding (PVS) mode to two-layered vortex shedding (TVS) mode for the flow past three tandem elliptic cylinders, the vortex center locations (x_c, y_c) are computed as

$$x_c = \frac{\int_S x\omega_z(x,y)dS}{\int_S \omega_z(x,y)dS}, y_c = \frac{\int_S y\omega_z(x,y)dS}{\int_S \omega_z(x,y)dS} \tag{20}$$

Where S is an area at which the vorticity strength $|\omega_z|$ is greater than the threshold value ($\beta\omega_{z,max}$, where $\omega_{z,max}$ is maximum value of $|\omega_z|$ in the vortex region and β varies in the range of $\beta = 0.2-0.4$).

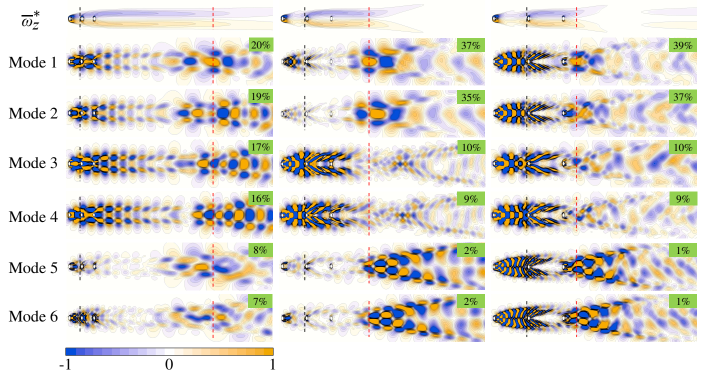

(a) (b) (c)

Figure 15: Top plot is time-averaged vorticity contour at $Re = 100$; second to bottom plots are spatial structures of vorticity POD modes. The first 70 diameters of the wake are shown. (a) $L/D = 3$; (b) $L/D = 6$; (c) $L/D = 8.5$. The black vertical dashed line is the boundary between primary and two-layered vortex shedding modes. The red vertical dashed line is the boundary between two-layered and secondary vortex shedding modes. Color bar is for the contours of fluctuating vorticity POD modes

The larger values of β determine the smaller sizes of vortex. Therefore, $\beta = 0.2$ is chosen in this paper for better vortex center computation. Based on the computed vortex center locations, a and h are calculated. The left side of Fig. 14 expresses variations of h/a with streamwise location x/D, Re and L/D; and the right side shows the associated wake structures with vertical dashed lines where $h/a = 0.365$. Several cases are examined, including $L/D = 3.0$ and $Re = 65$ (denoted as case A), $L/D = 3.5$ and $Re = 65$ (case B), $L/D = 2.5$ and $Re = 100$ (case C), and $L/D = 4$ and $Re = 100$ (case D). For case D, the h/a dramatically increases at first, then approaches the saturation at the value approximately close to 0.82 before the collapse of the primary vortex shedding mode. For case B, the h/a also increases with x/D and saturates at the value of 0.62; while for cases A and C the increase rates are fairly small. Interestingly, the increase rate of h/a depends significantly on L/D, at which the larger the L/D, the higher the increase rate. Apparently, the stability criteria of $h/a = 0.365$ discovered by Karasudani and Funakoshi[69] is broadly suitable in determining the first boundary; although the boundary location is at some streamwise location before the development of two-layered vortex shedding mode.

5.4 TVS−SVS transition

To examine the intermediate wake transition from two-layered vortex shedding mode to secondary vortex shedding (SVS) mode, the proper orthogonal decomposition (POD) method is utilized. The POD extracts the modal contents from a collection of snapshot data to capture the dominant structures. Specifically, when POD analyzes the velocity fields $\boldsymbol{u}^*(x, y, t)$, the modes (denoted as a basis function $\boldsymbol{\phi}_j(x, y)$, where j is the j^{th} mode number) spatially capture the structures with high fluctuations. In POD method proposed by Sirovich,[70] the fluctuations in the original flowfield are expressed as the

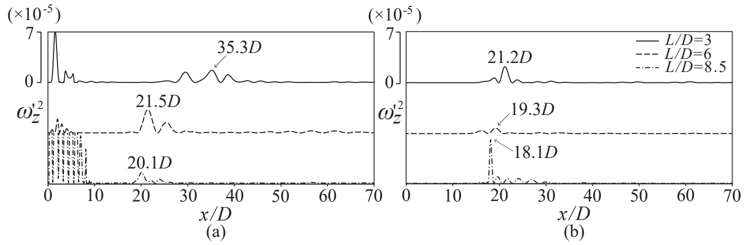

Figure 16: Distribution of square values of fluctuating vorticity along cylinder centerline for representative spacing ratios at (a): $Re = 100$ and (b): $Re = 160$. These values are extracted from POD mode 1

linear combination of the modes and their corresponding temporal coefficients $a_j(t)$

$$\boldsymbol{u}'(x,y,t) = \boldsymbol{u}^*(x,y,t) - \overline{\boldsymbol{u}}^*(x,y) = \sum_{j=1}^{M} a_j(t)\boldsymbol{\phi}_j(x,y) \tag{21}$$

where $\overline{\boldsymbol{u}}^*(x,y)$ is normalized time-averaged velocity fields ($\overline{\boldsymbol{u}}^*(x,y) = \overline{\boldsymbol{u}}(x,y)/U_\infty$); and M is the number of flowfield snapshots. The fluctuating velocity field data on the left hand side of equation (21) are arranged into the data matrix ($\boldsymbol{Y}(i,j)$) as follows

$$\boldsymbol{Y}(i,j) = [\boldsymbol{u}'(x_i, y_i, t_j)], i = 1, 2, ..., L, j = 1, 2, ..., M \tag{22}$$

where L is the number of grid nodes spatially distributed in the flowfield. Here, the snapshot method is utilized since the total snapshot number is much smaller than the dimension of an individual snapshot. Hence, the eigenvalues representing the amount of kinetic energy contribution hold by individual mode ($\boldsymbol{\phi}_j(x,y)$) are extracted from the equation (21). The eigenvalues are sorted in the order of importance to capture the physical structures with significantly fluctuating kinetic energy. In the present study, five hundred snapshots of instantaneous data in the interval of 50 time units, corresponding to approximately ten vortex shedding cycles of E1, are considered for the POD analysis. Fig. 15 depicts the first six flow structures of energetic POD modes at $Re = 100$. Since the POD analysis for fluctuating streamwise and transverse velocities presents identical flow physics with that for fluctuating vorticity (ω_z'), the field of ω_z' is utilized in the present study. The coherent structures visualized by the contour of ω_z' are presented with representative spacing ratios, including $L/D = 3.0$, 6.0, and 8.5. The boundaries separating vortex shedding modes identified in Fig. 8 are marked by vertical dashed lines.

In Fig. 15, the POD mode 1 is paired with the POD mode 2 due to their similar percentages of energy contribution, named as the first pair. Similarly, the second pair (modes 3 and 4) and third pair (modes 5 and 6) with similar structures and energy contribution percentages are also observed. The first and second paired modes contain 72% of total energy at $L/D = 3.0$, 91% at $L/D = 6.0$ and 95% at $L/D = 8.5$; while the first six modes contain 87% at $L/D = 3.0$, 95% at $L/D = 6.0$ and 97% at $L/D = 8.5$. Hence, within six modes, the flow instability corresponding to spatial structures is sufficiently captured. At $L/D = 3.0$, modes 1, 2, 3, and 4 show similar structures due to a slightly small difference in energy contribution percentages. The first paired modes and the second paired modes show the top-bottom symmetric contours with spatial harmonic structures about the cylinder centerline. The strengths of ω_z' distributed in the PVS mode are higher than those in the TVS and SVS modes. Hence, it reconfirms that the C_L frequencies of three cylinders are dominated by PVS mode. In addition, the sizes of the structures in the SVS mode are larger than those in the PVS and TVS modes, thus indicating the long streamwise wavelength vortices in the SVS mode and short streamwise wavelength vortices in the PVS and TVS modes. At $L/D = 6.0$, in the first paired modes, the intensive fluctuating vorticity strengths are distributed in PSV mode and through the second boundary. In addition, the dissipations are observed in the TVS mode and downstream region of SVS mode. Otherwise, the second paired modes express the strongly fluctuating vorticity structures in the PVS and TVS modes; while the weakly fluctuating vorticity structures are observed in the SVS mode. The second paired modes show the top-bottom symmetric structures in the PVS and TVS modes; while the third paired modes (modes 5 and 6) show top-bottom antisymmetric structures in the SVS mode. At $L/D = 8.5$, the distribution of the first paired modes and the second paired modes are similar to those at $L/D = 6.0$. However, in the third paired modes, the top-bottom antisymmetric vorticity structures are distributed in the PVS and SVS modes. Both the symmetricity and antisymmetricity show the flow nonlinearity. The symmetric fluctuating vorticity distributions indicate the regular periodicity of vortex shedding.

Fig. 16 depicts distribution of square values of fluctuating vorticity along cylinder centerline for representative spacing ratios, including $L/D = 3.0$, 6.0, and 8.5. These values are extracted from POD mode 1, which is the highest energetic mode. At $x/D > 10.0$, the locations of the second boundary are determined by the maximum peaks of ${\omega_z'}^2$, where the vortex paring event occurs. In Fig. 16a, at $Re = 100$, the second boundaries in the cases of $L/D = 3$, 6, and 8.5 are located at $35.3D$, $21.5D$, and $20.1D$ downstream, respectively. Hence, the locations of these second boundaries move upstream with an increase in L/D, which are the same as those observed in Fig. 8. In comparison with $Re = 100$, these second boundaries are located at shorter downstream distances from E1 at $Re = 160$ (Fig. 16b). That is because the vortices and their interactions are stronger at higher Reynolds numbers, urging the regular transition from TVS to SVS mode in the intermediate wake.

5.5 Flow irregularity

When the two-layered vortex shedding mode transitions into secondary vortex shedding mode in the intermediate wake, the instantaneous vorticity field becomes irregular (Fig. 8). On this transition, the vortices of opposite signs from two offset layers join in a pairing event, where the stretched vortex of weak strength intermittently and irregularly occurs (Fig. 11e). The vorticity irregularity is further presented in Fig. 17a and 17b by the spatial distribution of vortex centers. The locations of vortex centers are obtained from equation (20) by using 50 snapshots of vorticity field.

As shown in Fig. 17a, for $x/D \leq 16.2$, the centers of clockwise and counterclockwise vortices transport in two clearly separated trajectories on upper and lower sides of the wake centerline, respectively. For $x/D > 16.2$, the irregular interactions of same sign vortices occur in a paring event before intermediate wake transition at the second boundary ($x/D = 21.5$). After the transition, the vortices evolve along the streamwise and transverse directions, forming two spatial expansion regions. The blue and red inclined dashed lines present the envelopes for these regions, where the spatial expansion ratio is $y : x = 0.04$. It indicates the slow transverse expansion since the vortex strengths and interactions are weaker at lower Reynolds numbers. As a result, the clockwise and counterclockwise vortices arrange

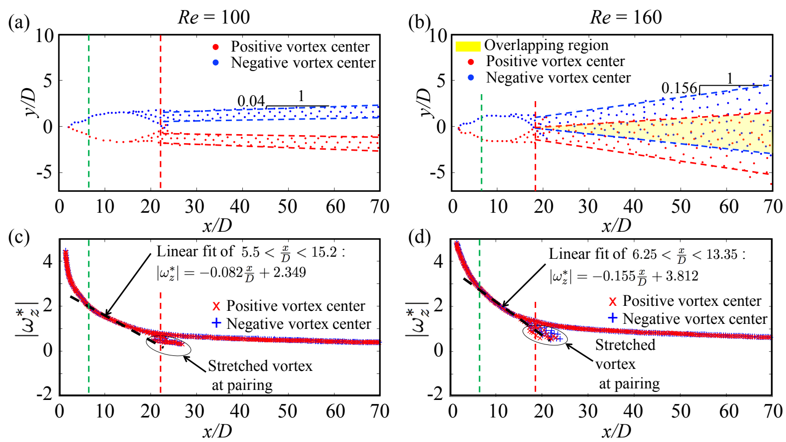

Figure 17: Spatial distribution of vortex centers at $Re = 100$ (a) and $Re = 160$ (b). The normalized vorticity strengths at $Re = 100$ (c) and $Re = 160$ (d). The spacing ratio is $L/D = 6.0$. The green vertical dashed line is the boundary between primary vortex shedding mode and two-layered vortex shedding mode. The red vertical dashed line is the boundary between two-layered vortex shedding mode and secondary vortex shedding mode. The blue and red inclined dashed lines present the envelops of the clockwise and counterclockwise vortex centers, respectively

themselves in their separated half-domains up to $x/D = 70$. Fig. 17c presents the normalized vorticity strengths of the vortex centers scattered in Fig. 17a. As the vortices evolve downstream, the vorticity strengths decay moderately as a function of streamwise location. For $x/D \leq 5.5$, the nonlinear decay of vortex strengths with x/D is observed in primary vortex shedding mode. For $5.5 < x/D < 15.2$, the linear decay of vortex strengths, $|\omega_z^*| = -0.082x^* + 2.349$, is observed in two-layered vortex shedding mode. The range of the linear decay includes the first boundary location ($x/D = 5.75$), where the near wake transition happens. That is because at this boundary the vortex pairing event does not occur. After passing the second boundary location at $x/D = 21.5$, some vortex strengths locate below the major curve due to the occurrence of stretched vortices at pairing. These reduced vortex strengths are because of the cross-annihilation of paired vortices of opposite signs.

As shown in Fig. 17b, for $x/D \leq 14.1$, the centers of clockwise and counterclockwise vortices transport in two clearly separated trajectories on two sides of the wake centerline, respectively. For $x/D > 14.1$, the irregular interactions of same sign vortices occur in a paring event before intermediate wake transition at the second boundary ($x/D = 19.3$). After the transition, the vortices evolve along the streamwise and transverse directions, forming two spatial expansion regions. In particular, while the clockwise vortices may join the lower side, counterclockwise vortices may join the upper side. The overlapping region occurs when two spatial regions expand transversely along two sides of the wake centerline. The blue and red inclined dashed lines present the envelopes for these regions, where the spatial expansion ratio is $y : x = 0.156$, which is approximately four times larger than that at $Re = 100$. Fig. 17d presents the normalized vorticity strengths of the vortex centers scattered in Fig. 17b. For $x/D \leq 6.25$, the nonlinear decay of vortex strengths with x/D is observed in primary vortex shedding mode. For $6.25 < x/D < 13.35$, the linear decay of vortex strengths is observed as $|\omega_z^*| =$

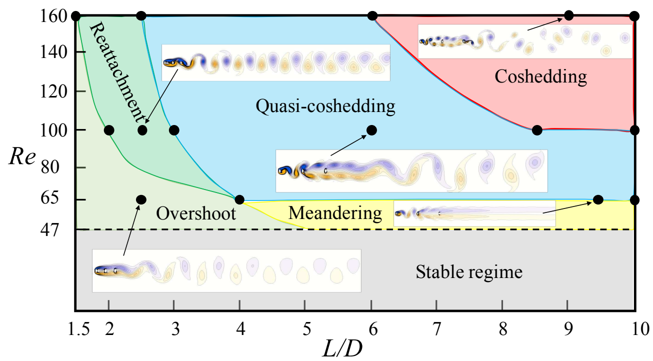

Figure 18: Flow regime map in the parametric space of $Re - L/D$. The boundary separating two adjacent flow regimes is determined using two adjacent midpoint data.

$-0.155x^* + 3.812$. The range of the linear decay includes the first boundary location ($x/D = 6.85$). After passing the second boundary location at $x/D = 19.3$, some vortex strengths locate below the major curve due to the occurrence of stretched vortices at pairing (as shown in Fig. 11e).

6 Flow dependence on Re and L/D

To summarize the interference of flow past three tandem elliptic cylinders, a map of distinct flow regimes in parametric space of $Re - L/D$ is produced in Fig. 18. The boundary separating two adjacent flow regimes is determined using two adjacent midpoint data. The stable flow regime appears when $Re \leq 47$;[64] while at $Re > 47$ the unstable flow is observed with five distinct regimes, including meandering, overshoot, reattachment, quasi-coshedding, and fully developed coshedding. The overshoot and coshedding regimes become apparent in low and high L/D regions, respectively. The reattachment regime is identified in a small-L/D and high-Re region; while the quasi-coshedding regime dominates the space of moderate-to-large L/D and Re. The meandering regime occurs in the space of low Re and moderate-to-large L/D. At $47 < Re \leq 65$, increasing L/D transforms the overshoot to meandering; while to reattachment and quasi-coshedding at $65 < Re \leq 160$. In high-Re region, the quasi-coshedding transforms into coshedding at moderate L/D; while in moderate-Re region the transformation is at sufficiently large L/D.

7 Conclusions

The flow around three elliptic cylinders in tandem arrangements was numerically conducted by using lattice Boltzmann method combined with block-structured topology-confined mesh refinement. The validations of the results were performed for two two-dimensional cases, such as an isolated circular cylinder and two side-by-side circular cylinders. The research points aim at the effects of cylinder spacing ratio and Reynolds number on the underlying fluid dynamics, including wake structures and hydrodynamics coefficients.

Five distinct flow regimes, depending on Re and L/D, are first revealed, as shown in Fig. 18: meandering ($47 < Re \leq 65$), overshoot ($1.0 \leq L/D \leq 2.0$), reattachment ($2.0 < L/D \leq 3.0$), quasi-coshedding ($3.0 < L/D < 8.5$), and coshedding ($8.5 \leq L/D \leq 10.0$). In meandering regime, the vortex transports with the mean flow velocity due to the high diffusivity of the flow at low Reynolds number. In overshoot regime, the lower and upper shear layers from the upstream cylinder overshoot the middle and downstream cylinders, introducing the stagnant flows. These shear layers further cross-annihilate each other behind downstream cylinder before forming a primary vortex shedding mode. In the reattachment regime, the vortices in primary vortex shedding mode form behind the upstream cylinder; and they alternately reattach and amalgamate with the same sign vortex shed from middle and downstream cylinders. In the quasi-coshedding regime, the primary vortex shedding mode occurs behind upstream cylinder and two-layered vortex shedding mode occurs behind middle and downstream cylinders. In the coshedding regime, the vortex sheddings are simultaneously evolved behind three elliptic cylinders. In particular, the upstream cylinder always exhibits primary vortex shedding mode; while two-layered and secondary vortex shedding modes are observed behind the middle and downstream cylinders, respectively.

Two boundaries corresponding to the first and second wake transitions are established by three approaches, including time-averaged transverse velocity field, vortex identification, and proper orthogonal decomposition. At the first boundary, vortices divert from the cylinder centerline following two layers; while the vortices converge the cylinder centerline at the second boundary. The vortex convergence induces the irregular occurrence of stretched vortex in a pairing event as a result of the interaction between two vortices of opposite signs. Hence, the movement of second boundary originates from the location, at which the stretched vortex occurs. The location of the first boundary is not stationary and depends on the location of middle cylinder in the range of $Re = 65 - 100$; while it is stationary in front of middle cylinder at $Re = 160$. Otherwise, the second boundaries move upstream with an increase in L/D; while the movement range increases with a decrease in Re. That is because the level of disturbances is lower at lower Reynolds numbers.

The tandem arrangement induces the drag reduction of three elliptic cylinders in the whole range of spacing ratio, where the drag coefficients of three cylinders are below that of single cylinder. In overshoot regime, the stagnant flows signify the tiny reduction of mean drag coefficient of upstream cylinder; while keeping significant increase in mean drag coefficient of downstream cylinder. The mean drag coefficient of middle cylinder is negative due to its sandwiched position between two stagnant flows. When the overshoot transforms into the reattachment, the mean drag coefficients of middle cylinder dramatically increase from negative to positive value, signifying the drag inversion region. Otherwise, the critical spacing ratio is observed when the mean drag and lift coefficients of three cylinders express a sharp jump at the border between the reattachment and the quasi-coshedding. In the quasi-coshedding regime, the mean drag and lift coefficients of upstream cylinder increase tinily; and they approach those of single circular cylinder at sufficiently large spacing ratio, suggesting small effect of middle and downstream cylinders on upstream cylinder. In coshedding regime, the mean drag coefficient of downstream cylinder drastically increases due to the existence of secondary vortex shedding mode. The vortex shedding frequencies of three cylinders are identical in the range of $L/D = 1.5 - 8.0$ due to the existence of primary vortex shedding mode. For $8.5 \leq L/D \leq 10.0$, the vortex shedding frequency of downstream cylinder sharply drops due to the appearance of secondary vortex shedding mode in the intermediate wake.

Acknowledgments

We are deeply grateful to all the anonymous reviewers for their invaluable, detailed and informative suggestions and comments on the drafts of this article. We would also like to express our special thanks to Mr. Kazuaki Uchibori at Institute of Computational Fluid Dynamics (iCFD) for the fruitful discussions about High Performance Computing and Lattice Boltzman Method.

Declaration of interest

The authors declare no competing financial interest.

DATA AVAILABILITY

The data that support the findings of this study are available from the corresponding author upon reasonable request.

References

[1] M. Lahooti and D. Kim, “Unsteady concentration transport over an array of cylinders in low-reynolds-number flow,” *Phys. Fluids*, vol. 32, no. 5, p. 053602, 2020.

[2] T. Tang, P. Yu, X. Shan, J. Li, and S. Yu, “On the transition behavior of laminar flow through and around a multi-cylinder array,” *Phys. Fluids*, vol. 32, no. 1, p. 013601, 2020.

[3] W.-Y. Chang, G. Constantinescu, and W.-F. Tsai, “Effect of array submergence on flow and coherent structures through and around a circular array of rigid vertical cylinders,” *Phys. Fluids*, vol. 32, no. 3, p. 035110, 2020.

[4] M. Liu, W. Huai, B. Ji, and P. Han, “Numerical study on the drag characteristics of rigid submerged vegetation patches,” *Phys. Fluids*, vol. 33, no. 8, p. 085123, 2021.

[5] M. Liu, W. Huai, and B. Ji, “Characteristics of the flow structures through and around a submerged canopy patch,” *Phys. Fluids*, vol. 33, no. 3, p. 035144, 2021.

[6] V. Nguyen, T. Nguyen-Thoi, and V. Duong, “Characteristics of the flow around four cylinders of various shapes,” *Ocean Eng.*, vol. 238, p. 109690, 2021.

[7] K. Kingora, W. L. Burks, and H. Sadat, “Flow and mass transfer characteristics for interacting side-by-side cylinders,” *Phys. Fluids*, vol. 34, no. 2, p. 023602, 2022.

[8] H. Eizadi, H. An, T. Zhou, H. Zhu, and L. Cheng, “Wake transitions of six tandem circular cylinders at low reynolds numbers,” *Phys. Fluids*, vol. 34, no. 2, p. 023605, 2022.

[9] M. Zhang and Z. C. Zheng, “Relations of POD modes and lyapunov exponents to the nonlinear dynamic states in flow over oscillating tandem cylinders,” *Phys. Fluids*, vol. 30, no. 12, p. 123602, 2018.

[10] Q. Zhou, M. M. Alam, S. Cao, H. Liao, and M. Li, "Numerical study of wake and aerodynamic forces on two tandem circular cylinders at $Re = 10^3$," *Phys. Fluids*, vol. 31, no. 4, p. 045103, 2019.

[11] L. Chen and Y. Dong, "Numerical investigation on fluid forces of piggyback circular cylinders in tandem arrangement at low reynolds numbers," *Acta Mech. Sin.*, pp. 1–14, 2021.

[12] W. A. Khan, J. Culham, and M. M. Yovanovich, "Fluid flow around and heat transfer from elliptical cylinders: analytical approach," *J. thermophys. heat transf.*, vol. 19, no. 2, pp. 178–185, 2005.

[13] M. Zdravkovich, "Review of flow interference between two circular cylinders in various arrangements," *J. Heat Transf.*, vol. 99, no. 4, pp. 618–633, 1977.

[14] T. Igarashi, "Characteristics of the flow around two circular cylinders arranged in tandem: 1st report," *Bull. JSME*, vol. 24, no. 188, pp. 323–331, 1981.

[15] T. Igarashi, "Characteristics of the flow around two circular cylinders arranged in tandem: 2nd report, unique phenomenon at small spacing," *Bull. JSME*, vol. 27, no. 233, pp. 2380–2387, 1984.

[16] T. Igarashi and K. Suzuki, "Characteristics of the flow around three circular cylinders," *Bull. JSME*, vol. 27, no. 233, pp. 2397–2404, 1984.

[17] M. M. Alam, M. Moriya, K. Takai, and H. Sakamoto, "Fluctuating fluid forces acting on two circular cylinders in a tandem arrangement at a subcritical Reynolds number," *J. Wind Eng. Ind. Aerodyn.*, vol. 91, no. 1-2, pp. 139–154, 2003.

[18] D. Sumner, "Two circular cylinders in cross-flow: a review," *J. Fluids Struct.*, vol. 26, no. 6, pp. 849–899, 2010.

[19] M. Zdravkovich, "The effects of interference between circular cylinders in cross flow," *J. Fluids Struct.*, vol. 1, no. 2, pp. 239–261, 1987.

[20] G. V. Papaioannou, D. K. Yue, M. S. Triantafyllou, and G. E. Karniadakis, "Three-dimensionality effects in flow around two tandem cylinders," *J. Fluid Mech.*, vol. 558, pp. 387–413, 2006.

[21] L. Ljungkrona, C. Norberg, and B. Sunden, "Free-stream turbulence and tube spacing effects on surface pressure fluctuations for two tubes in an in-line arrangement," *J. Fluids Struct.*, vol. 5, no. 6, pp. 701–727, 1991.

[22] L. Ljungkrona and B. Sundén, "Flow visualization and surface pressure measurement on two tubes in an inline arrangement," *Exp. Therm. Fluid Sci.*, vol. 6, no. 1, pp. 15–27, 1993.

[23] B. Carmo and J. Meneghini, "Numerical investigation of the flow around two circular cylinders in tandem," *J. Fluids Struct.*, vol. 22, no. 6-7, pp. 979–988, 2006.

[24] M. M. Alam, "The aerodynamics of a cylinder submerged in the wake of another," *J. Fluids Struct.*, vol. 51, pp. 393–400, 2014.

[25] W. Yang and M. A. Stremler, "Critical spacing of stationary tandem circular cylinders at $Re \approx 100$," *J. Fluids Struct.*, vol. 89, pp. 49–60, 2019.

[26] C.-H. Liu and J. M. Chen, "Observations of hysteresis in flow around two square cylinders in a tandem arrangement," *J. Wind Eng. Ind. Aerodyn.*, vol. 90, no. 9, pp. 1019–1050, 2002.

[27] G. Xu and Y. Zhou, "Strouhal numbers in the wake of two inline cylinders," *Exp. Fluids*, vol. 37, no. 2, pp. 248–256, 2004.

[28] T. Kitagawa and H. Ohta, "Numerical investigation on flow around circular cylinders in tandem arrangement at a subcritical reynolds number," *J. Fluids Struct.*, vol. 24, no. 5, pp. 680–699, 2008.

[29] R. Wang, H. Zhu, Y. Bao, D. Zhou, H. Ping, Z. Han, and H. Xu, "Modification of three-dimensional instability in the planar shear flow around two circular cylinders in tandem," *Phys. Fluids*, vol. 31, no. 10, p. 104110, 2019.

[30] M. Grioni, S. Elaskar, and A. Mirasso, "A numerical study of the flow interference between two circular cylinders in tandem by scale-adaptive simulation model," *J. Appl. Fluid Mech.*, vol. 13, no. 1, pp. 169–183, 2020.

[31] S. Mittal, V. Kumar, and A. Raghuvanshi, "Unsteady incompressible flows past two cylinders in tandem and staggered arrangements," *Int. J. Numer. Methods Fluids*, vol. 25, no. 11, pp. 1315–1344, 1997.

[32] J. Meneghini, F. Saltara, C. Siqueira, and J. Ferrari Jr, "Numerical simulation of flow interference between two circular cylinders in tandem and side-by-side arrangements," *J. Fluids Struct.*, vol. 15, no. 2, pp. 327–350, 2001.

[33] S. Singha and K. Sinhamahapatra, "High-resolution numerical simulation of low Reynolds number incompressible flow about two cylinders in tandem," *J. Fluids Eng.*, vol. 132, no. 1, 2010.

[34] B. Carmo, J. Meneghini, and S. Sherwin, "Possible states in the flow around two circular cylinders in tandem with separations in the vicinity of the drag inversion spacing," *Phys. Fluids*, vol. 22, no. 5, p. 054101, 2010.

[35] H. Zhu, J. Zhong, and T. Zhou, "Wake structure characteristics of three tandem circular cylinders at a low Reynolds number of 160," *Phys. Fluids*, vol. 33, no. 4, p. 044113, 2021.

[36] M. M. Alam and Y. Zhou, "Strouhal numbers, forces and flow structures around two tandem cylinders of different diameters," *J. Fluids Struct.*, vol. 24, no. 4, pp. 505–526, 2008.

[37] Y. Gao, S. Etienne, D. Yu, X. Wang, and S. Tan, "Bi-stable flow around tandem cylinders of different diameters at low Reynolds number," *Fluid Dyn. Res.*, vol. 43, no. 5, p. 055506, 2011.

[38] T. Igarashi, "Characteristics of a flow around two circular cylinders of different diameters arranged in tandem," *Bull. JSME*, vol. 25, no. 201, pp. 349–357, 1982.

[39] M.-m. Liu, "The predominant frequency for viscous flow past two tandem circular cylinders of different diameters at low Reynolds number," *Proc. Inst. Mech. Eng. M: J. Eng. Marit. Environ.*, vol. 234, no. 2, pp. 534–546, 2020.

[40] L. Wang, M. M. Alam, and Y. Zhou, "Two tandem cylinders of different diameters in cross-flow: Effect of an upstream cylinder on wake dynamics," *J. Fluid Mech.*, vol. 836, pp. 5–42, 2018.

[41] M. M. Alam, M. Elhimer, L. Wang, D. L. Jacono, and C. Wong, “Vortex shedding from tandem cylinders,” *Exp. Fluids*, vol. 59, no. 3, pp. 1–17, 2018.

[42] X. Shan, “Effect of an upstream cylinder on the wake dynamics of two tandem cylinders with different diameters at low Reynolds numbers,” *Phys. Fluids*, vol. 33, no. 8, p. 083605, 2021.

[43] X. Shi, M. Alam, and H. Bai, “Wakes of elliptical cylinders at low reynolds number,” *Int. J. Heat Fluid Flow*, vol. 82, p. 108553, 2020.

[44] V. Pulletikurthi, I. Paul, K. Prakash, and B. Prasad, “On the development of low frequency structures in near and far laminar wakes,” *Phys. Fluids*, vol. 31, no. 2, p. 023604, 2019.

[45] J. Zhu, L. E. Holmedal, D. Myrhaug, and H. Wang, “Near-wall effect on flow around an elliptic cylinder translating above a plane wall,” *Phys. Fluids*, vol. 32, no. 9, p. 093607, 2020.

[46] J. Zhu and L. E. Holmedal, “A numerical study of separation and stagnation points for steady and unsteady flow over an elliptic cylinder near a moving wall,” *Phys. Fluids*, vol. 33, no. 8, p. 083617, 2021.

[47] J. Zhu, F. Jiang, and L. E. Holmedal, “Three-dimensional wake transition behind an elliptic cylinder near a moving wall,” *Phys. Fluids*, vol. 33, no. 4, p. 043606, 2021.

[48] X. Wu, F. Chen, and S. Zhou, “Stationary and flow-induced vibration of two elliptic cylinders in tandem by immersed boundary-MRT lattice Boltzmann flux solver,” *J. Fluids Struct.*, vol. 91, p. 102762, 2019.

[49] X. Wu, Y. Li, and S. Zhou, “Flow-induced vibration on isolated and tandem elliptic cylinders with varying reduced velocities: A lattice Boltzmann flux solver study with immersed boundary method,” *Eur. J. Mech. B Fluids*, vol. 89, pp. 45–63, 2021.

[50] P. Vorobieff, D. Georgiev, and M. S. Ingber, “Onset of the second wake: dependence on the Reynolds number,” *Phys. Fluids*, vol. 14, no. 7, pp. L53–L56, 2002.

[51] S. Chen and G. D. Doolen, “Lattice boltzmann method for fluid flows,” *Annu. Rev. Fluid Mech.*, vol. 30, no. 1, pp. 329–364, 1998.

[52] P. Lallemand and L.-S. Luo, “Theory of the lattice Boltzmann method: Dispersion, dissipation, isotropy, Galilean invariance, and stability,” *Phys. Rev. E*, vol. 61, no. 6, p. 6546, 2000.

[53] K. Uchibori and T. Tamura, “LES study on aerodynamics of auto-rotating square flat plate by IBM and SAMR,” *J. Fluids Struct.*, vol. 89, pp. 108–122, 2019.

[54] N. Jansson, R. Bale, K. Onishi, and M. Tsubokura, “CUBE: A scalable framework for large-scale industrial simulations,” *Int. J. High Perform. Comput. Appl.*, vol. 33, no. 4, pp. 678–698, 2019.

[55] M. Bader, *Space-filling curves*, vol. 9. Computational Science and Engineering, Springer Berlin Heidelberg, 2013.

[56] M. Rohde, D. Kandhai, J. Derksen, and H. E. Van den Akker, “A generic, mass conservative local grid refinement technique for lattice-Boltzmann schemes,” *Int. J. Numer. Methods Fluids*, vol. 51, no. 4, pp. 439–468, 2006.

[57] A. J. Ladd, "Numerical simulations of particulate suspensions via a discretized Boltzmann equation. Part 1. Theoretical foundation," *J. Fluid Mech*, vol. 271, pp. 285–309, 1994.

[58] M. Bouzidi, M. Firdaouss, and P. Lallemand, "Momentum transfer of a Boltzmann-lattice fluid with boundaries," *Phys. Fluids*, vol. 13, no. 11, pp. 3452–3459, 2001.

[59] D. Yu, R. Mei, L.-S. Luo, and W. Shyy, "Viscous flow computations with the method of lattice Boltzmann equation," *Prog. Aerosp. Sci.*, vol. 39, no. 5, pp. 329–367, 2003.

[60] Q. Zheng and M. M. Alam, "Intrinsic features of flow past three square prisms in side-by-side arrangement," *J. Fluid Mech.*, vol. 826, pp. 996–1033, 2017.

[61] L. Qu, C. Norberg, L. Davidson, S.-H. Peng, and F. Wang, "Quantitative numerical analysis of flow past a circular cylinder at Reynolds number between 50 and 200," *J. Fluids Struct.*, vol. 39, pp. 347–370, 2013.

[62] W. Chen, C. Ji, M. M. Alam, J. Williams, and D. Xu, "Numerical simulations of flow past three circular cylinders in equilateral-triangular arrangements," *J. Fluid Mech.*, vol. 891, 2020.

[63] C. H. Williamson, "Oblique and parallel modes of vortex shedding in the wake of a circular cylinder at low Reynolds numbers," *J. Fluid Mech.*, vol. 206, pp. 579–627, 1989.

[64] C. Norberg, "Flow around a circular cylinder: aspects of fluctuating lift," *J. Fluids Struct.*, vol. 15, no. 3-4, pp. 459–469, 2001.

[65] Y. Bao, D. Zhou, and J. Tu, "Flow characteristics of two in-phase oscillating cylinders in side-by-side arrangement," *Comput. Fluids*, vol. 71, pp. 124–145, 2013.

[66] D. S. Lee, M. Y. Ha, H. S. Yoon, and S. Balachandar, "A numerical study on the flow patterns of two oscillating cylinders," *J. Fluids Struct.*, vol. 25, no. 2, pp. 263–283, 2009.

[67] M. C. Thompson, A. Radi, A. Rao, J. Sheridan, and K. Hourigan, "Low-Reynolds-number wakes of elliptical cylinders: from the circular cylinder to the normal flat plate," *J. Fluid Mech.*, vol. 751, pp. 570–600, 2014.

[68] M. Zdravkovich, "Review of interference-induced oscillations in flow past two parallel circular cylinders in various arrangements," *J. Wind Eng. Ind. Aerodyn.*, vol. 28, no. 1-3, pp. 183–199, 1988.

[69] T. Karasudani and M. Funakoshi, "Evolution of a vortex street in the far wake of a cylinder," *Fluid Dyn. Res.*, vol. 14, no. 6, p. 331, 1994.

[70] L. Sirovich, "Turbulence and the dynamics of coherent structures. I. Coherent structures," *Q. Appl. Math.*, vol. 45, no. 3, pp. 561–571, 1987.

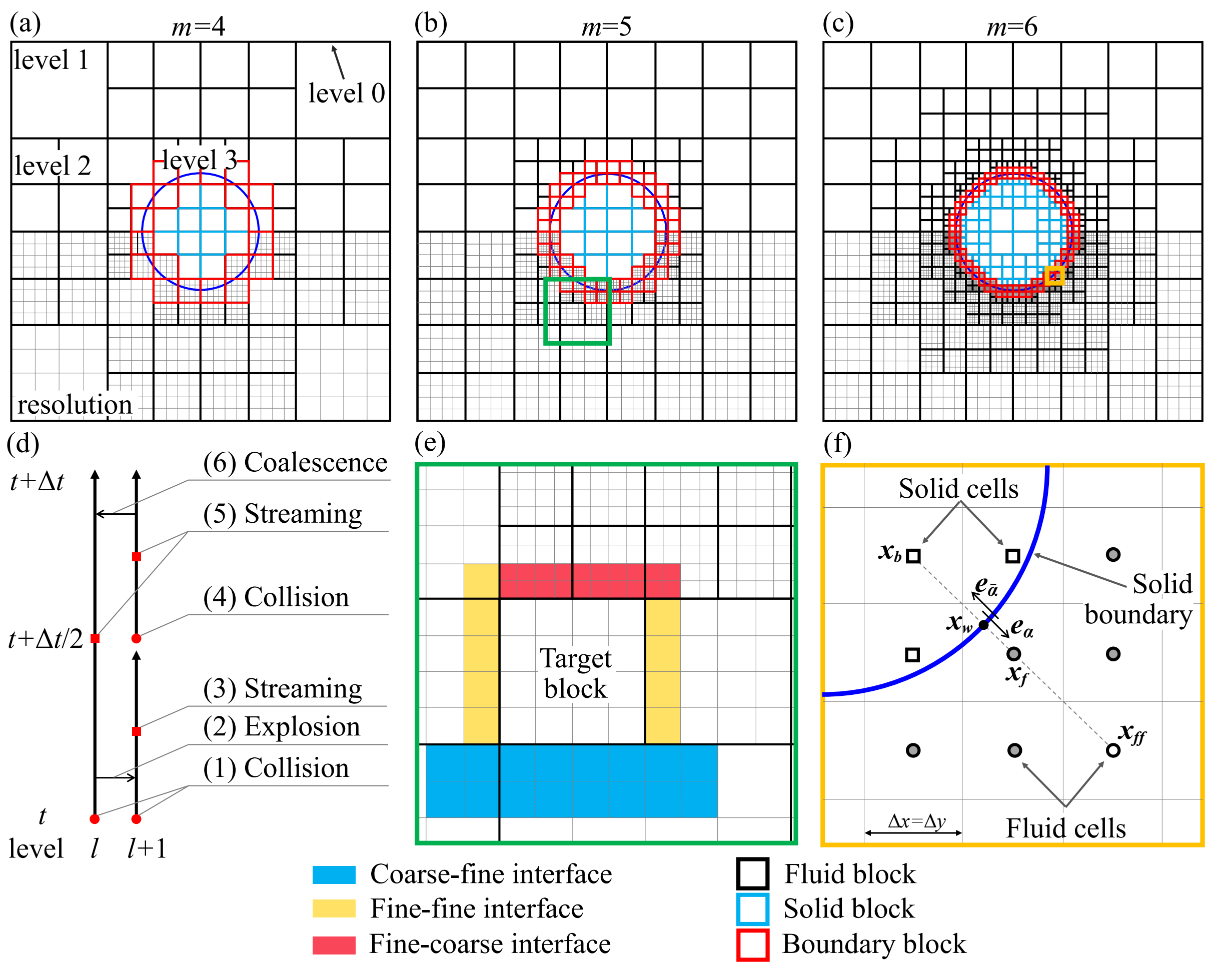
(a)
m=4
level 1
level 0
level 2
level 3
resolution
(b)
m=5
(c)
m=6
(d)
t+Δt
t+Δt/2
t
level
l
l+1
(6) Coalescence
(5) Streaming
(4) Collision
(3) Streaming
(2) Explosion
(1) Collision
(e)
Target block
(f)
Solid cells
Solid boundary
Fluid cells
Δx=Δy
Coarse-fine interface
Fine-fine interface
Fine-coarse interface
Fluid block
Solid block
Boundary block

PLEASE CITE THIS ARTICLE AS DOI: 10.1063/5.0086685

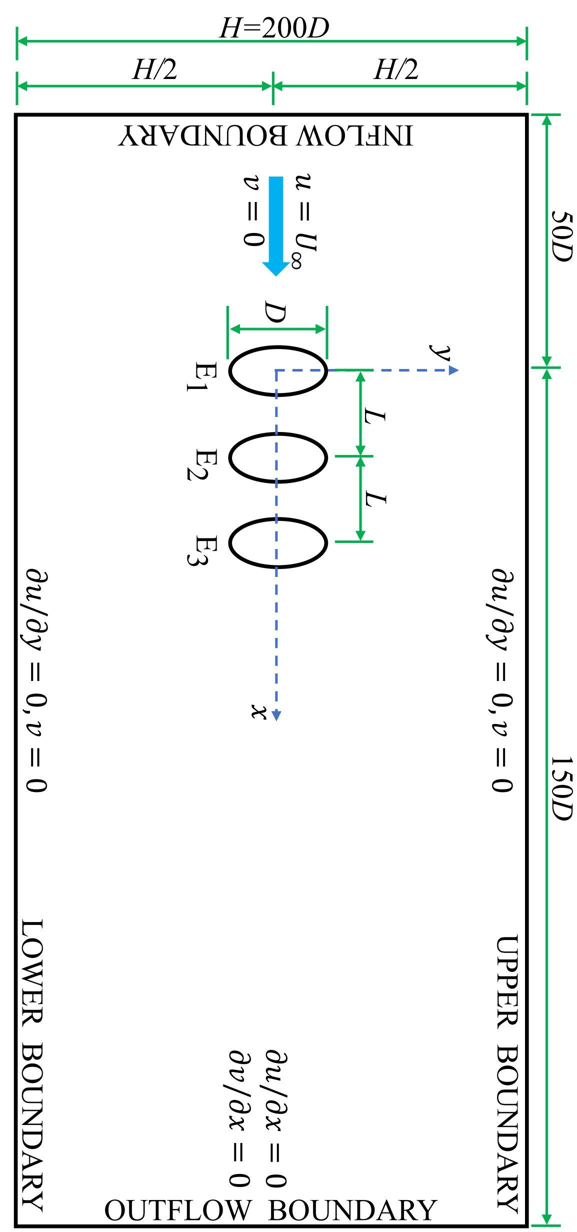

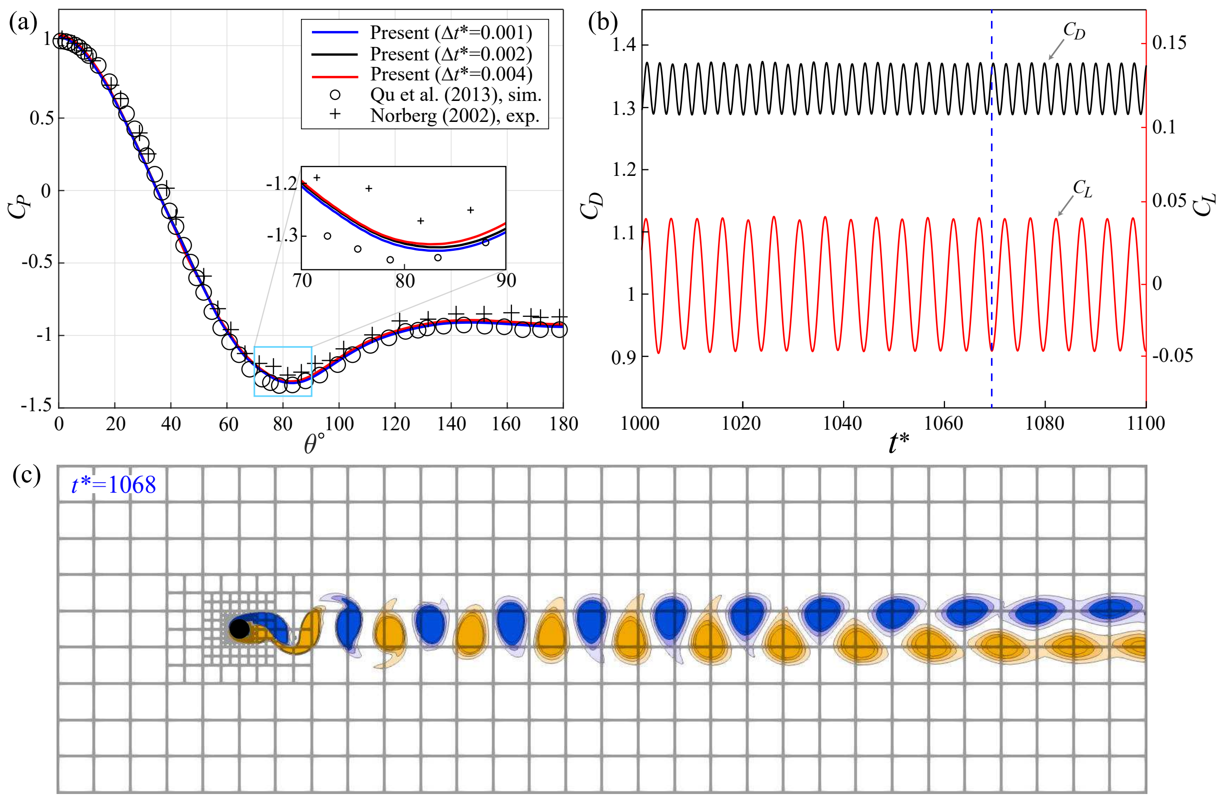
(a)
Present (Δt*=0.001)
Present (Δt*=0.002)
Present (Δt*=0.004)
Qu et al. (2013), sim.
Norberg (2002), exp.
C_P
$\theta°$
(b)
C_D
C_L
t^*
(c)
t^*=1068

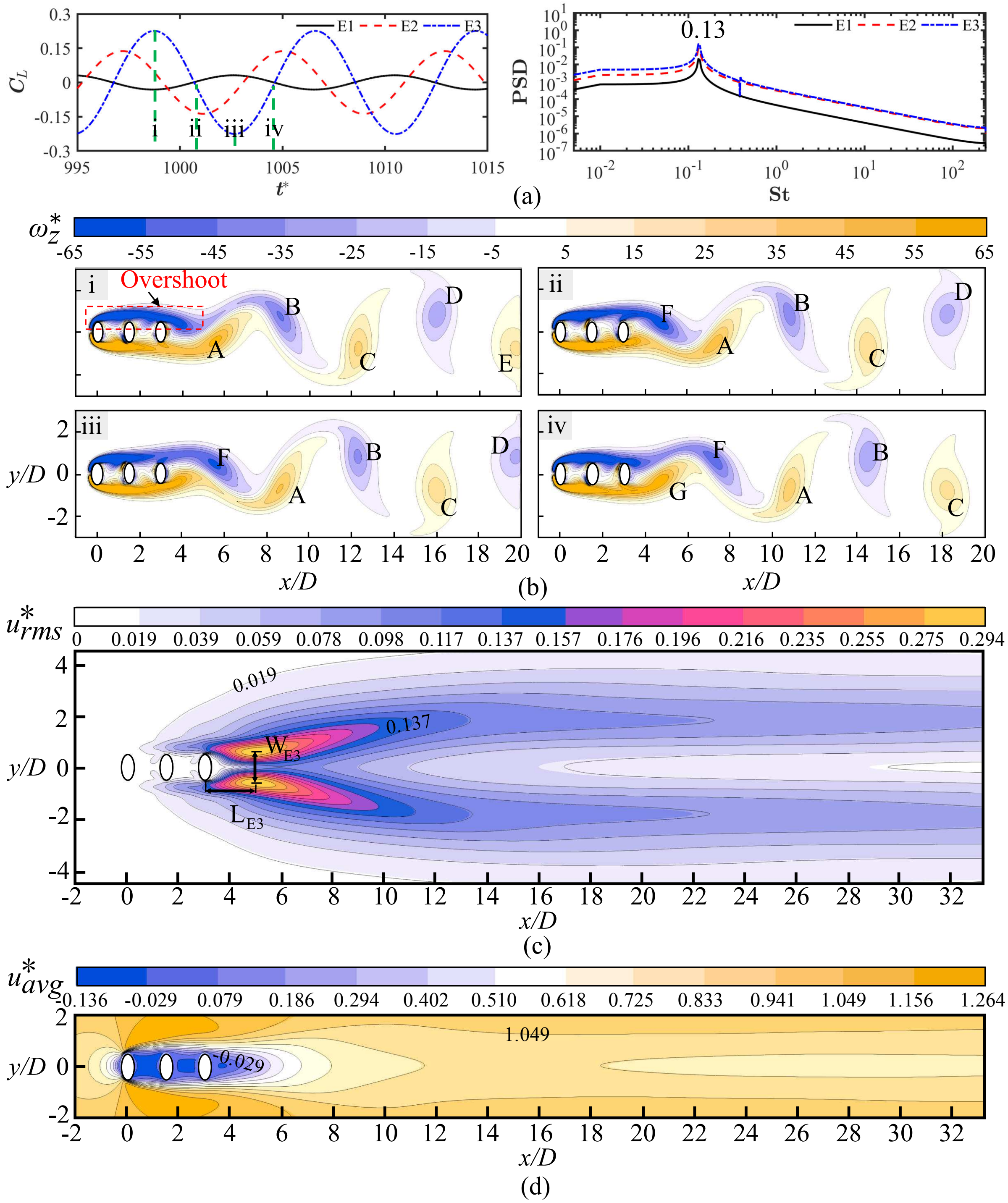
C_L
E1
E2
E3
i
ii
iii
iv
t^*
(a)
PSD
0.13
St
ω_z^*
Overshoot
A
B
C
D
E
F
G
y/D
x/D
(b)
u_{rms}^*
0.019
0.137
W_{E3}
L_{E3}
(c)
u_{avg}^*
1.049
-0.029
(d)

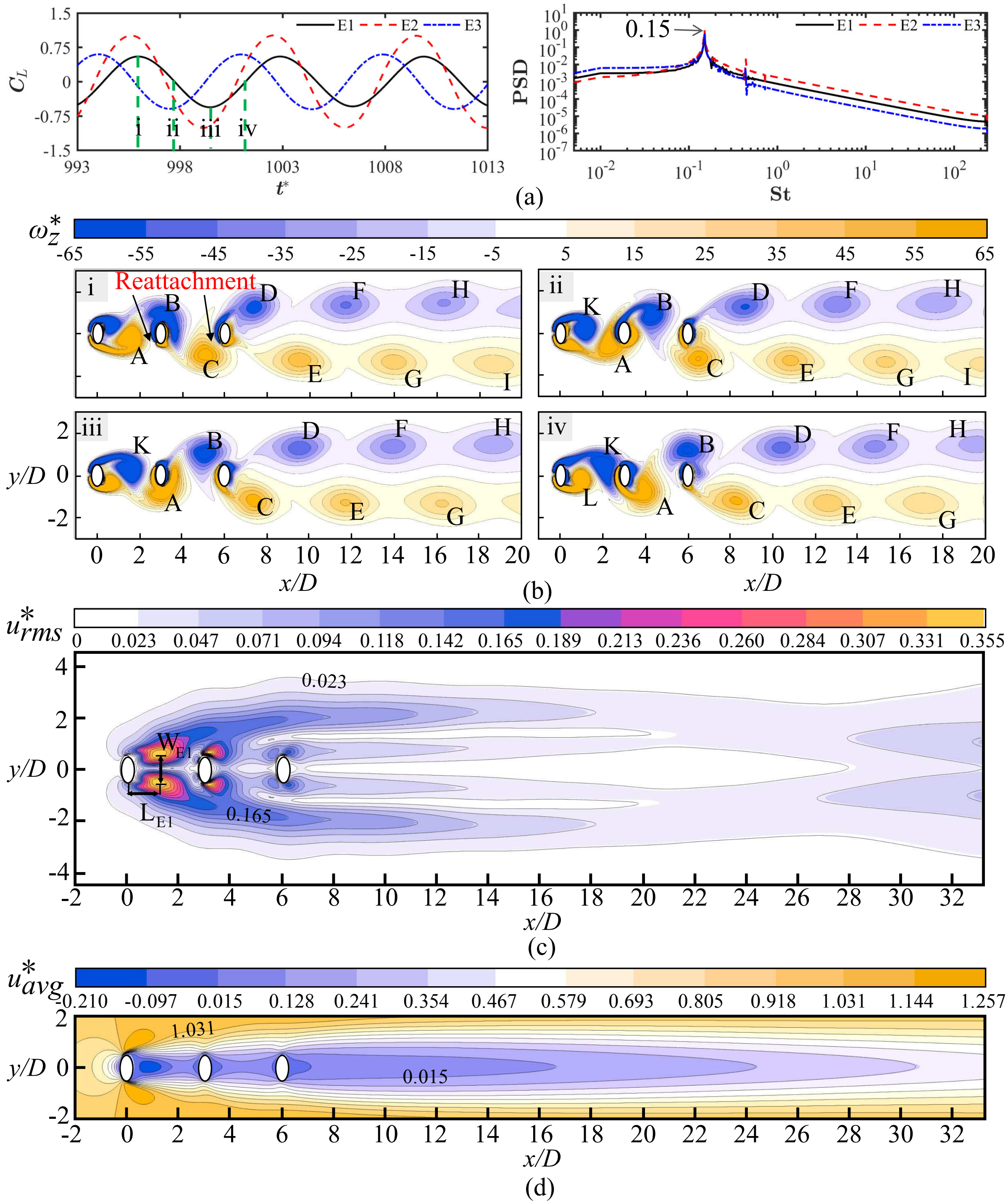
C_L
E1
E2
E3
i
ii
iii
iv
t^*
(a)
PSD
0.15
St
ω_z^*
Reattachment
A
B
C
D
E
F
G
H
I
K
L
y/D
x/D
(b)
u_{rms}^*
0.023
0.165
W_{E1}
L_{E1}
(c)
u_{avg}^*
1.031
0.015
(d)

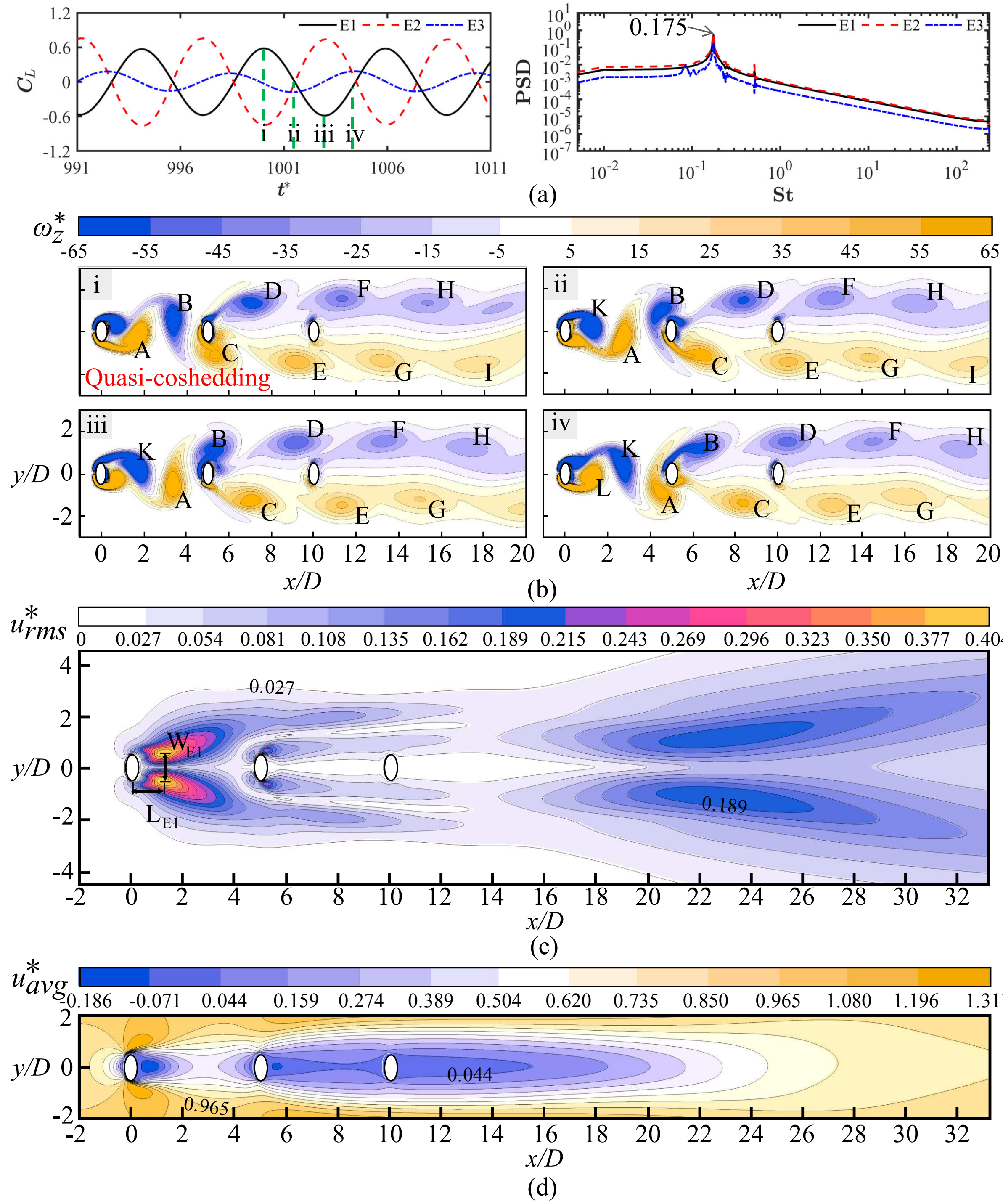
E1
E2
E3
0.175
PSD
St
(a)
Quasi-coshedding
(b)
0.027
0.189
W_{E1}
L_{E1}
(c)
0.044
0.965
(d)

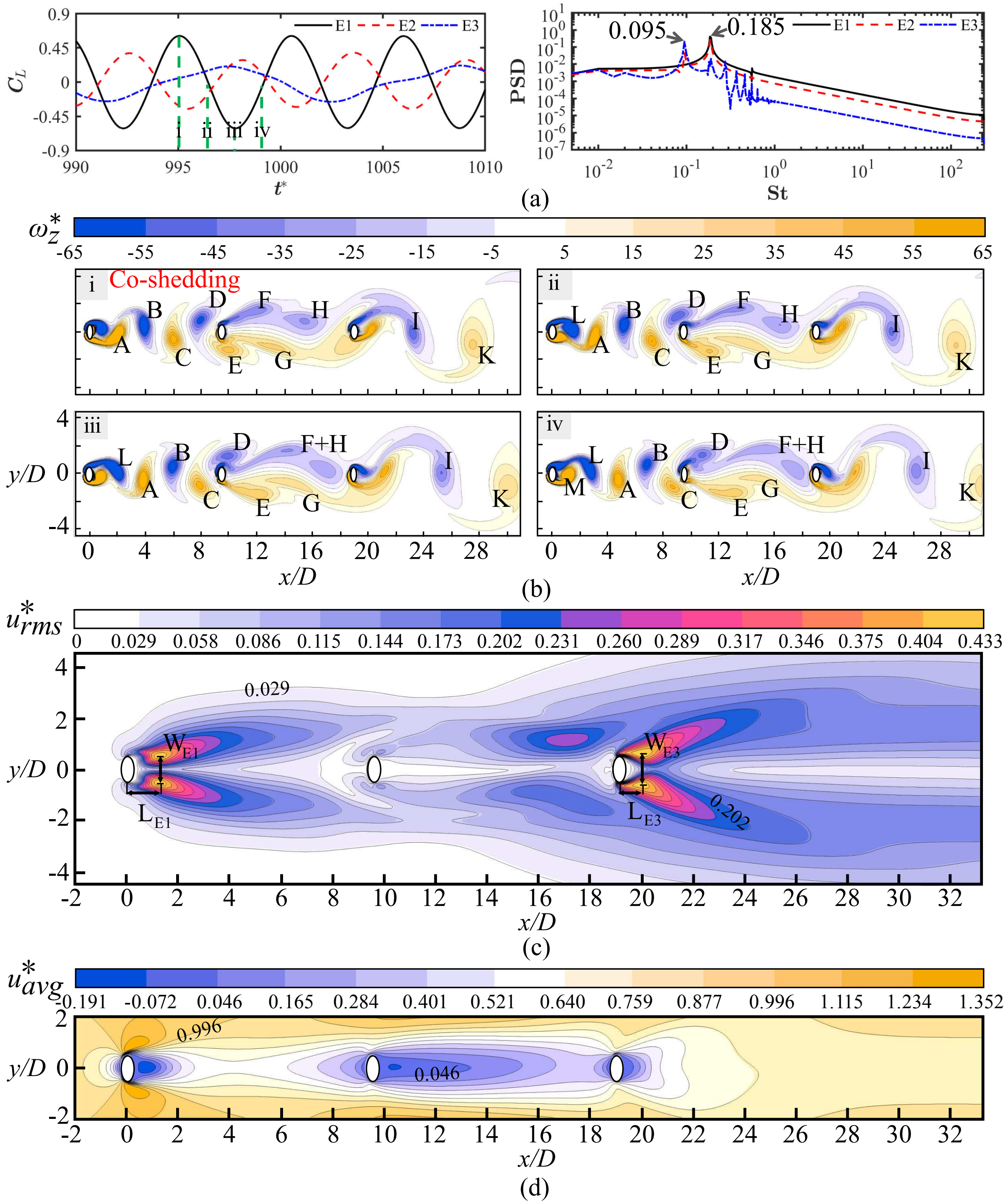
C_L
E1
E2
E3
i
ii
iii
iv
t^*
PSD
0.095
0.185
St
(a)
ω_z^*
Co-shedding
y/D
x/D
(b)
u^*_{rms}
0.029
0.202
W_{E1}
L_{E1}
W_{E3}
L_{E3}
(c)
u^*_{avg}
0.996
0.046
(d)

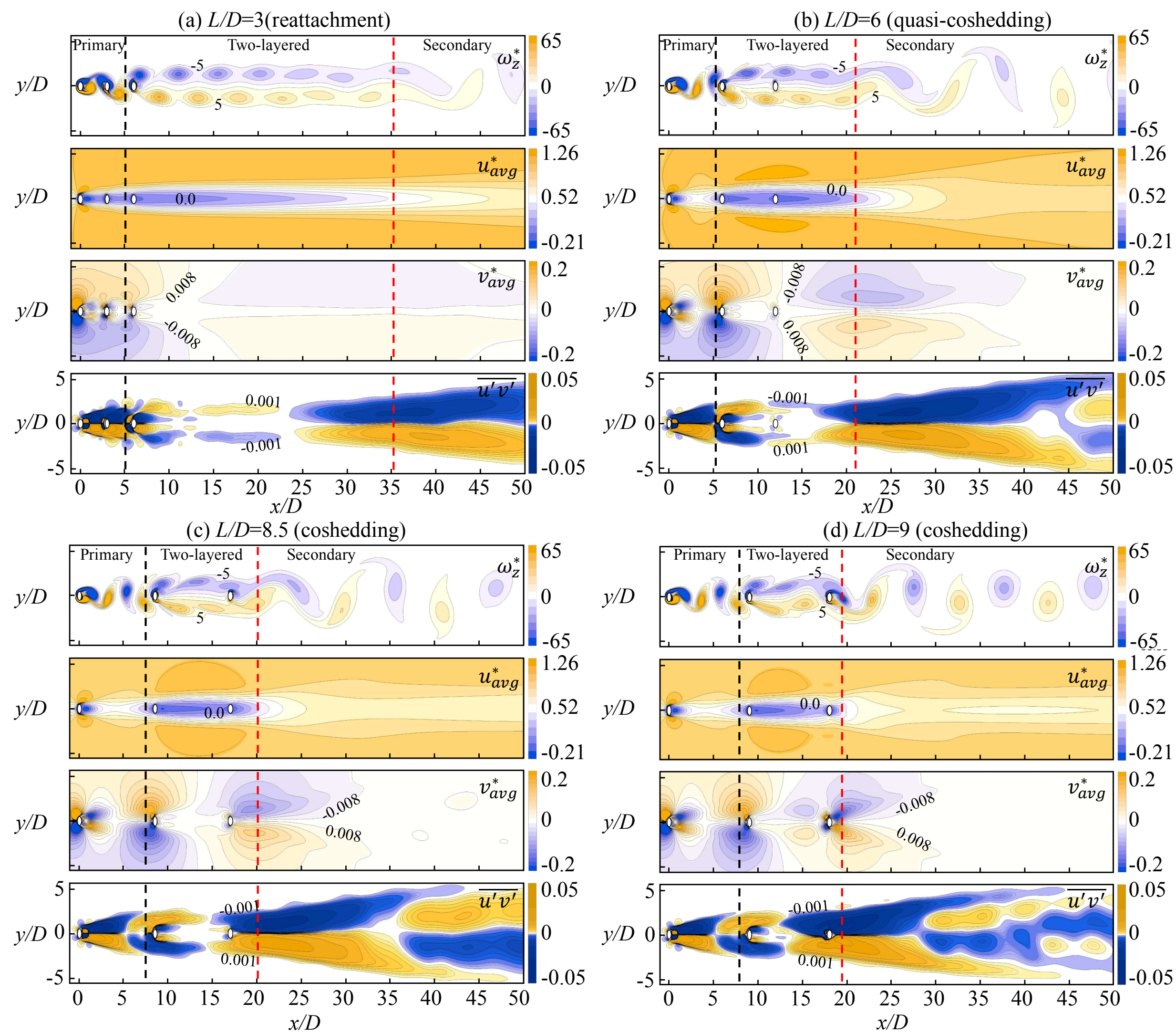
(a) L/D=3(reattachment)
(b) L/D=6 (quasi-coshedding)
(c) L/D=8.5 (coshedding)
(d) L/D=9 (coshedding)
Primary
Two-layered
Secondary
y/D
x/D
ω*z
u*avg
v*avg
u'v'
65
0
-65
1.26
0.52
-0.21
0.2
-0.2
0.05
-0.05
0.0
0.008
-0.008
0.001
-0.001
5
-5
0
10
15
20
25
30
35
40
45
50

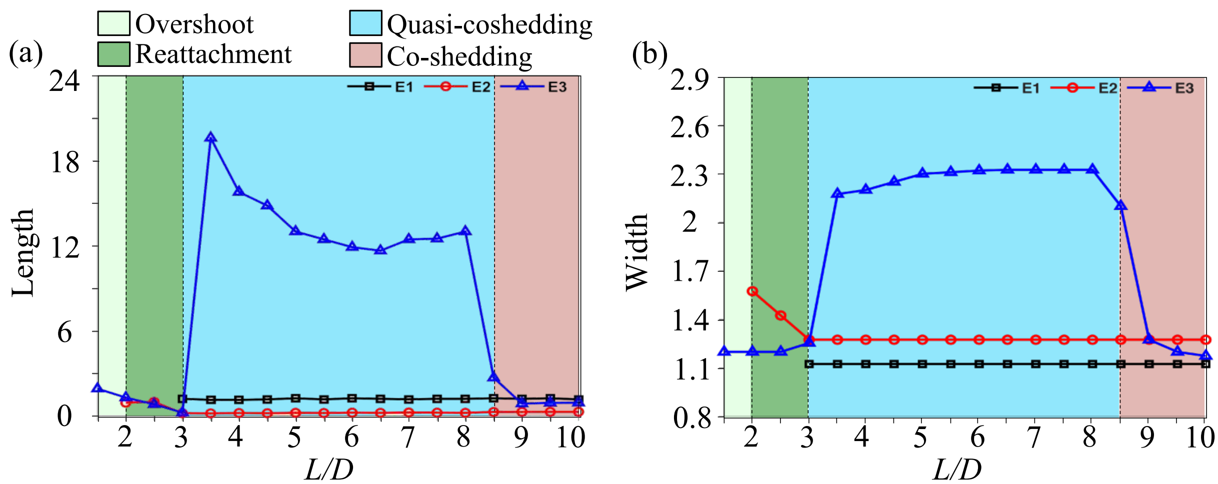
Overshoot
Reattachment
Quasi-coshedding
Co-shedding
(a)
(b)
Length
Width
L/D
E1
E2
E3

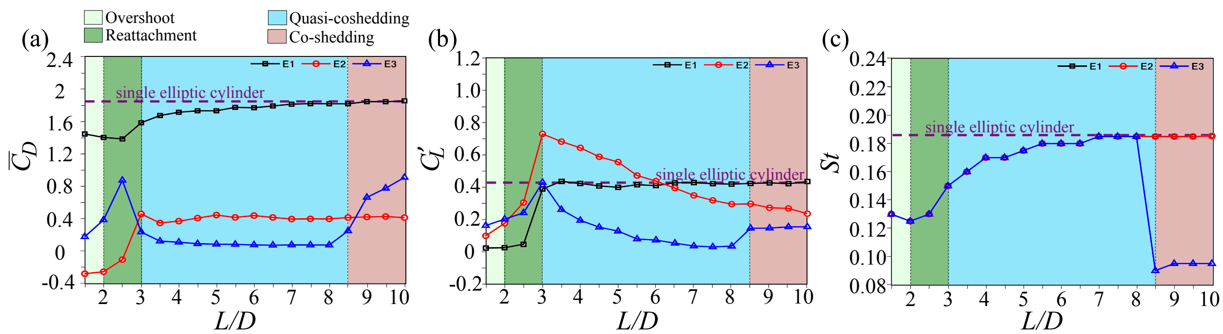
Overshoot
Reattachment
Quasi-coshedding
Co-shedding
(a)
(b)
(c)
E1
E2
E3
single elliptic cylinder
$\overline{C}_D$
C_L'
St
L/D

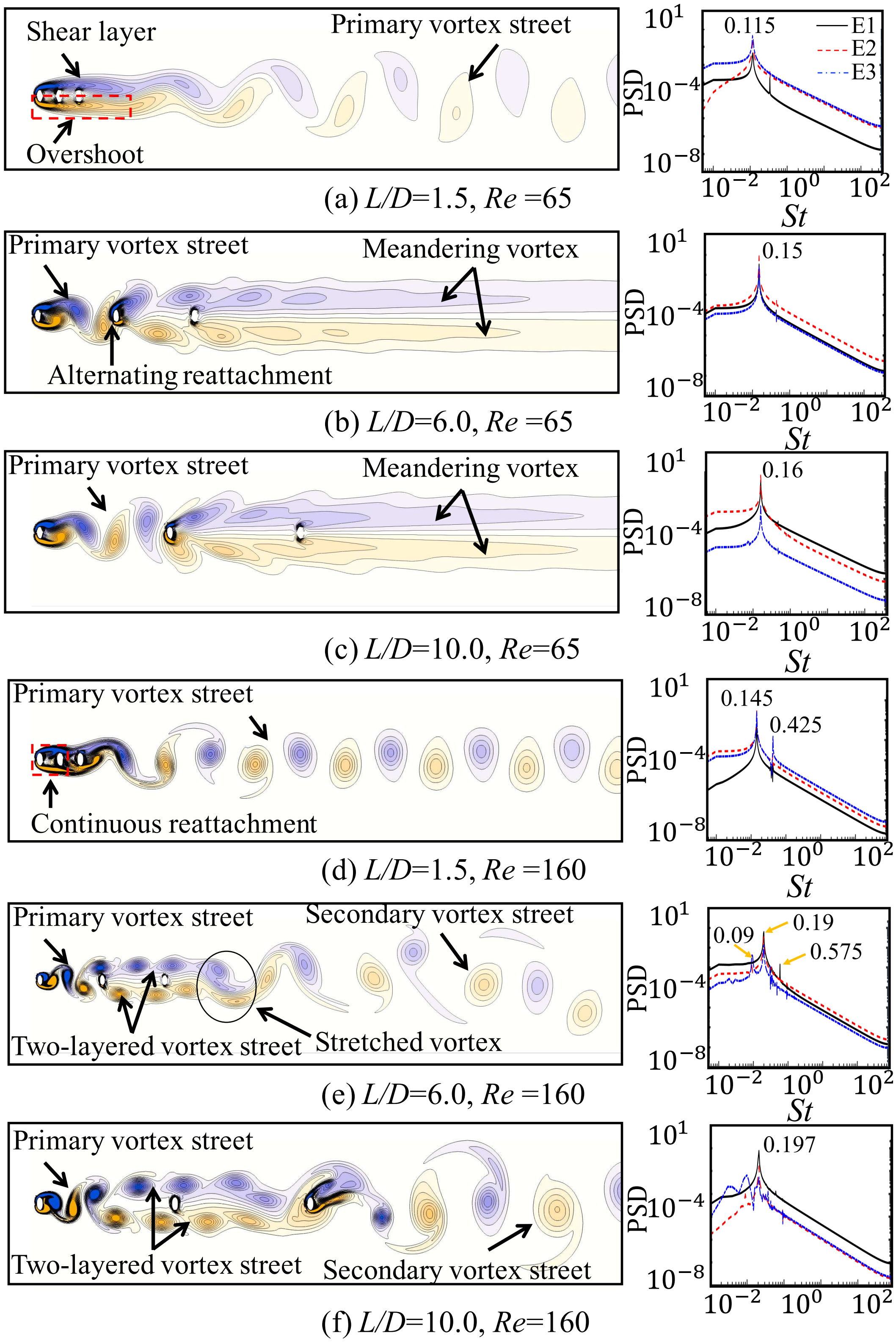
Shear layer
Primary vortex street
Overshoot
0.115
E1
E2
E3
PSD
St
(a) L/D=1.5, Re =65
Primary vortex street
Meandering vortex
Alternating reattachment
0.15
(b) L/D=6.0, Re =65
Primary vortex street
Meandering vortex
0.16
(c) L/D=10.0, Re=65
Primary vortex street
Continuous reattachment
0.145
0.425
(d) L/D=1.5, Re =160
Primary vortex street
Secondary vortex street
Two-layered vortex street
Stretched vortex
0.09
0.19
0.575
(e) L/D=6.0, Re =160
Primary vortex street
Two-layered vortex street
Secondary vortex street
0.197
(f) L/D=10.0, Re=160

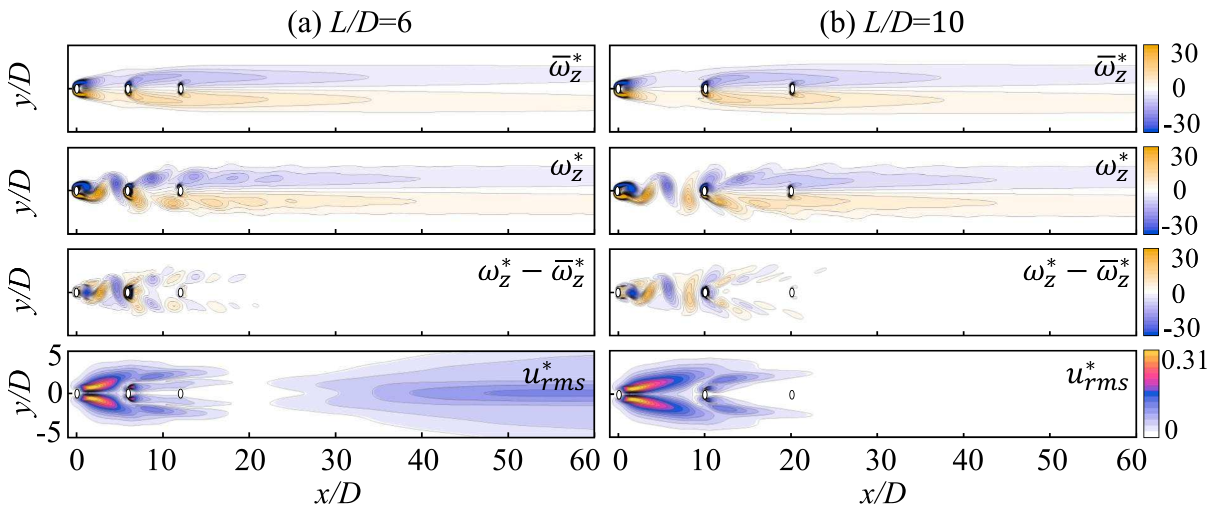
(a) L/D=6
(b) L/D=10
$\overline{\omega}_z^*$
ω_z^*
$\omega_z^* - \overline{\omega}_z^*$
u_{rms}^*
y/D
x/D
30
0
-30
0.31
0
5
-5
0 10 20 30 40 50 60

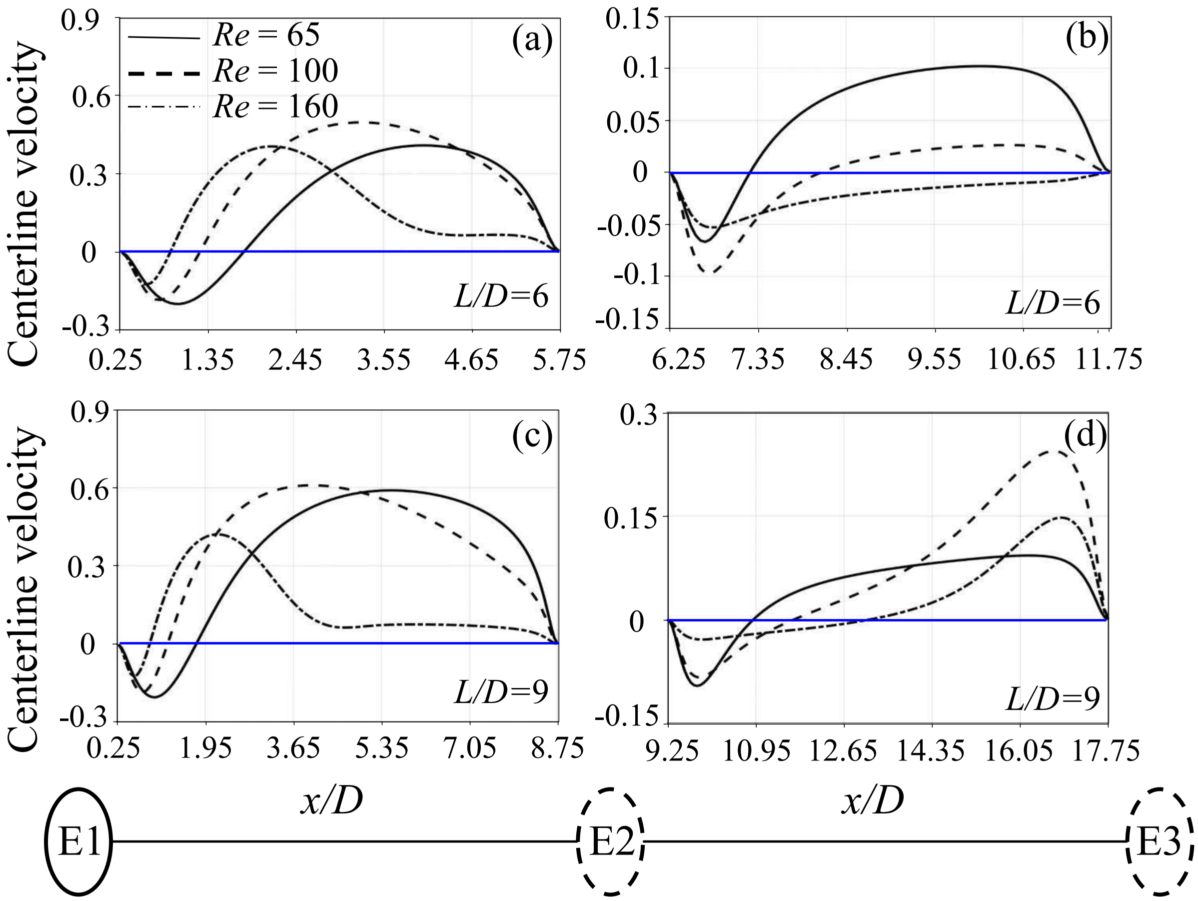
Re = 65
Re = 100
Re = 160
(a)
(b)
(c)
(d)
L/D=6
L/D=6
L/D=9
L/D=9
Centerline velocity
Centerline velocity
x/D
x/D
E1
E2
E3

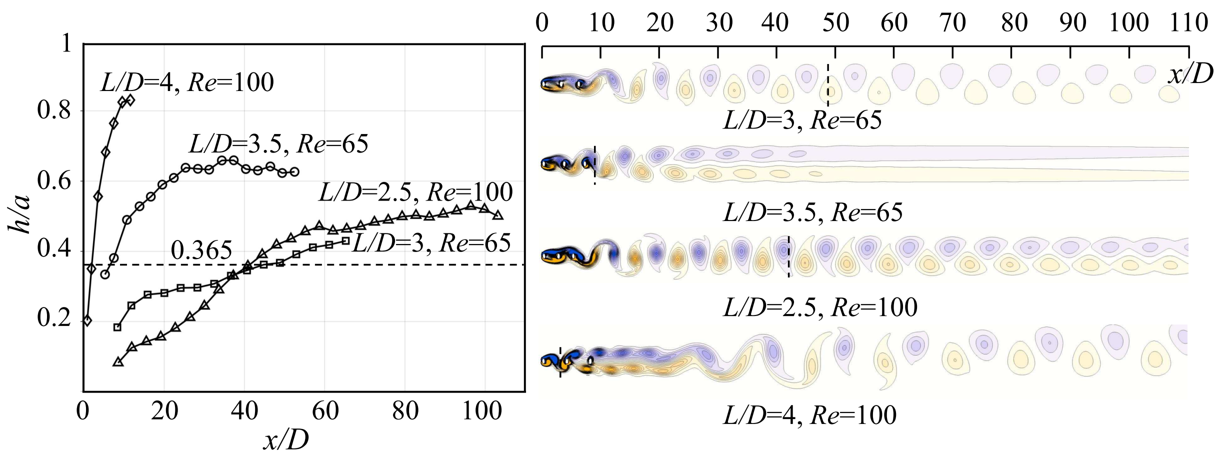
L/D=4, Re=100
L/D=3.5, Re=65
L/D=2.5, Re=100
L/D=3, Re=65
0.365
h/a
x/D
0
0.2
0.4
0.6
0.8
1
20
40
60
80
100
0 10 20 30 40 50 60 70 80 90 100 110
x/D
L/D=3, Re=65
L/D=3.5, Re=65
L/D=2.5, Re=100
L/D=4, Re=100

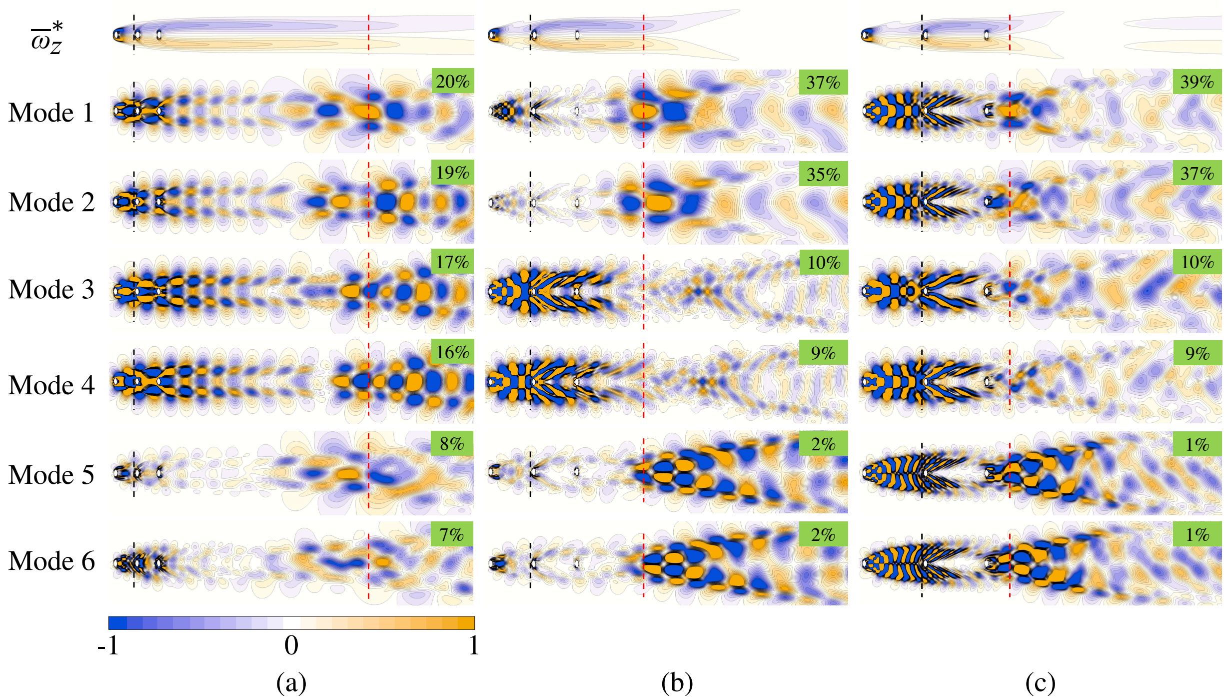
$\overline{\omega}_z^*$
Mode 1
Mode 2
Mode 3
Mode 4
Mode 5
Mode 6
20%
19%
17%
16%
8%
7%
37%
35%
10%
9%
2%
2%
39%
37%
10%
9%
1%
1%
-1
0
1
(a)
(b)
(c)

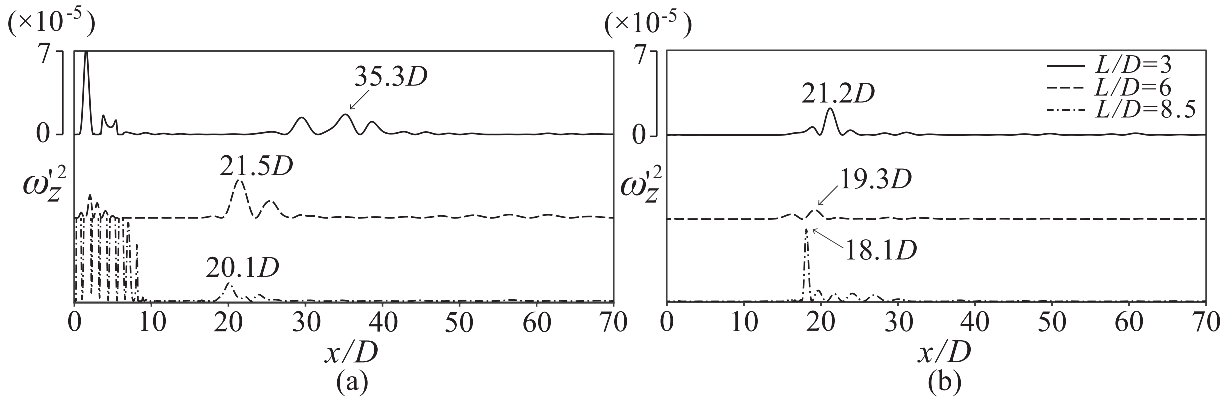
(×10^-5)
7
0
35.3D
21.5D
20.1D
ω'z^2
0 10 20 30 40 50 60 70
x/D
(a)
(×10^-5)
7
0
21.2D
19.3D
18.1D
L/D=3
L/D=6
L/D=8.5
0 10 20 30 40 50 60 70
x/D
(b)

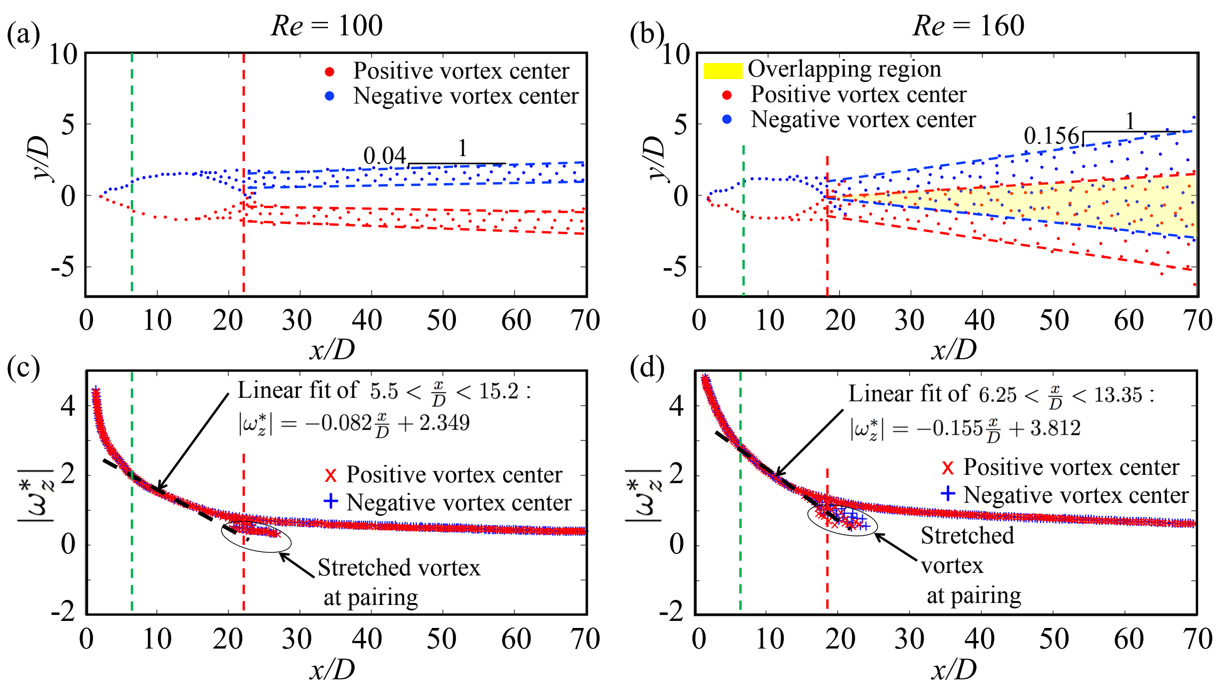
(a)
Re = 100
Positive vortex center
Negative vortex center
0.04
1
y/D
x/D
(b)
Re = 160
Overlapping region
Positive vortex center
Negative vortex center
0.156
1
y/D
x/D
(c)
Linear fit of $5.5 < \frac{x}{D} < 15.2$:
$|\omega_z^*| = -0.082\frac{x}{D} + 2.349$
Positive vortex center
Negative vortex center
Stretched vortex
at pairing
$|\omega_z^*|$
x/D
(d)
Linear fit of $6.25 < \frac{x}{D} < 13.35$:
$|\omega_z^*| = -0.155\frac{x}{D} + 3.812$
Positive vortex center
Negative vortex center
Stretched
vortex
at pairing
$|\omega_z^*|$
x/D

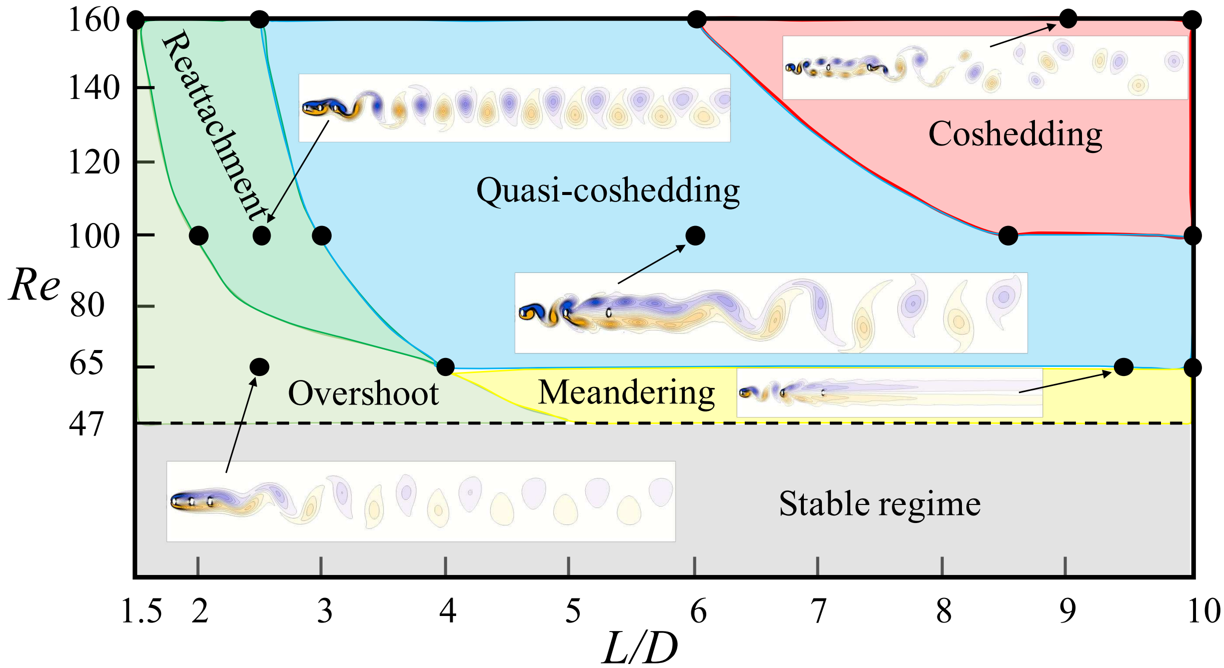
160
140
120
100
80
65
47
Re
1.5
2
3
4
5
6
7
8
9
10
L/D
Reattachment
Quasi-coshedding
Coshedding
Overshoot
Meandering
Stable regime